Molybdenum silicide (nano)materials for ^{99}Mo/^{99m}Tc generator applications

Master Thesis

D. B. Keijzer

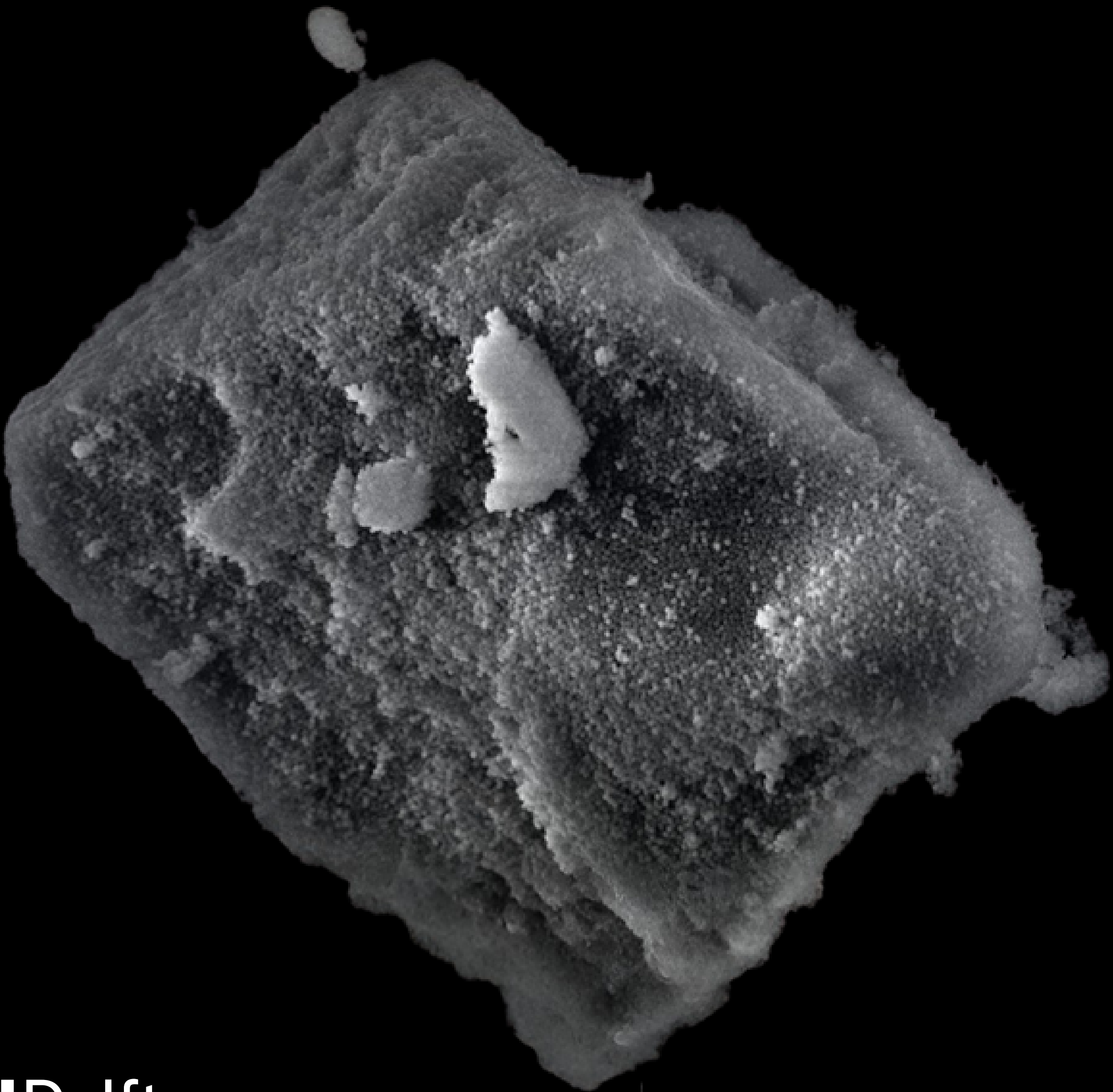

Delft University of Technology

Molybdenum silicide (nano)materials for ^{99}Mo/^{99m}Tc generator applications

Designing and investigating molybdenum silicide (nano)materials as targets for neutron activated $^{99}\mathrm{Mo}$ production for $^{99}\mathrm{Mo}/^{99m}\mathrm{Tc}$ generator applications

by

D. B. Keijzer

to obtain the degree of Master of Science

at the Delft University of Technology,

to be defended publicly on Wednesday, January 29, 2025 at 15:00 PM.

Student number:	5422361
Project duration:	September 2, 2024 – January 29, 2025
Supervisor:	Dr. ir. R. M. de Kruijff
Daily supervisor:	Gauri
Thesis committee:	Dr. ir. R. M. de Kruijff
	Dr. ir. A. G. Denkova
	Dr. E. M. Kelder

Cover: Scanning electron microscope image of the synthesized SiO_2 precursor.

TUDelft

Acknowledgements

First and foremost, I want to thank my daily supervisor, Gauri, for all her help during my thesis. She taught me the ins and outs of the lab, answered all my questions patiently, and kept thinking in possibilities even when I kept finding myself in situations like furnaces breaking down. Thanks to you, my furnace-cleaning skills have greatly improved! I would also like to thank my supervisor, Robin de Kruijff. The biweekly meetings were incredibly useful for keeping my project on track, and your input on the challenges I faced was greatly appreciated. I am sorry once again for being your most expensive student so far — hopefully, I will hold the record for a while. A big thank you to Antonia Denkova and Erik Kelder for being part of my thesis committee and for dedicating your time to my work. I also want to thank the technicians from ARI: Astrid van der Meer, Baukje Terpstra, Eline van den Heuvel and Folkert Geurink. And to Anna, Jaap, Meeke and Özkan, thanks for all the (much-needed) coffee breaks and for keeping my spirits up when things didn't go as planned. Finally, I want to thank my family and friends for your endless encouragement over the last five months, even though most of the time you had absolutely no idea what I was talking about.

Thank you all for being part of this adventure — it wouldn't have been the same without you!

Damian Keijzer
Delft, January 2025

Abstract

The radionuclide technetium-99m ($^{99m}\mathrm{Tc}$) is utilized in 80-85% of in-vivo nuclear medicine diagnostics due to its ideal physical and chemical properties, including a short half-life, gamma emission suitable for imaging, and versatile chemistry. Its production relies on molybdenum-99 ($^{99}\mathrm{Mo}$), traditionally generated through uranium fission. However, the transition to low-enriched uranium (LEU) targets and growing demand for $^{99m}\mathrm{Tc}$ have driven the search for alternative production methods and materials. This study investigates the potential of molybdenum silicide ($MoSi_2$) materials as targets for neutron-activated $^{99}\mathrm{Mo}$ production and as generators for $^{99m}\mathrm{Tc}$ extraction. Three synthesis methods were explored to produce nanoscale molybdenum silicides. A sol-gel carbothermic reduction method failed to produce $MoSi_2$, yielding elemental molybdenum, molybdenum dioxide, and molybdenum carbide due to oxygen contamination. The sol-gel preoxidation method successfully coated commercial $MoSi_2$ with an amorphous silica layer, enhancing the material's stability. The magnesiothermic reduction method successfully produced an oxide mixture intermediate (SiO_2/MoO_3) with nanosphere structures, initially containing 0.57 wt% molybdenum. The molybdenum content was later increased to 23.96 wt%. However, synthesis of the Si/$MoSi_2$ nanocomposites from this intermediate was not completed due to time constraints. The chemical stability, extraction and retention behavior of commercial and silica-coated $MoSi_2$ were evaluated in MilliQ and methyl ethyl ketone (MEK). The silica coating reduced molybdenum leaching and exhibited selective $^{99m}\mathrm{Tc}$ extraction. Retention studies highlighted the significant role of solvent interactions in governing radionuclide adsorption. In MEK, the silica-coated material exhibited lower $^{99m}\mathrm{Tc}$ retention, likely due to reduced adsorption sites caused by solvent interactions with silanol groups, while $^{99}\mathrm{Mo}$ retention could not be evaluated due to insufficient extraction data. The results demonstrate the potential of silica-coated $MoSi_2$ in $^{99}\mathrm{Mo}$/$^{99m}\mathrm{Tc}$ generator applications. However, further work is needed to optimize synthesis, increase surface area and evaluate long-term performance under irradiation. This could pave the way for sustainable and efficient isotope production systems.

Contents

Acknowledgements . . . iii

Abstract . . . v

Abbreviations . . . ix

List of Figures . . . xi

List of Tables . . . xiii

1 Introduction . . . 1

2 Theoretical Background . . . 5
  2.1 Production of ^{99}Mo . . . 5
    2.1.1 Fission-produced ^{99}Mo . . . 5
    2.1.2 Neutron-capture-produced ^{99}Mo . . . 5
    2.1.3 Accelerator-based ^{99}Mo production . . . 6
  2.2 Production of ^{99m}Tc (^{99}Mo/^{99m}Tc generator) . . . 7
  2.3 Utilizing hot atom chemistry principles . . . 9
  2.4 Fundamentally different ^{99}Mo/^{99m}Tc generator . . . 10
  2.5 Molybdenum silicides . . . 10
  2.6 Measurement techniques . . . 12
    2.6.1 Brunauer-Emmett-Teller (BET) analysis . . . 12
    2.6.2 Fourier-Transform Infrared Spectroscopy (FTIR) . . . 12
    2.6.3 Germanium gamma counter . . . 12
    2.6.4 Inductively Coupled Plasma Mass Spectrometry (ICP-MS) . . . 12
    2.6.5 Scanning Electron Microscopy (SEM) . . . 12
    2.6.6 Transmission Electron Microscopy (TEM) . . . 13
    2.6.7 X-Ray Diffraction (XRD) . . . 13

3 Materials & Methods . . . 15
  3.1 Materials & Devices . . . 15
  3.2 Material synthesis . . . 16
    3.2.1 Characterization . . . 17
  3.3 Stability tests . . . 17
  3.4 Irradiation experiments . . . 18
    3.4.1 ^{99}Mo and ^{99m}Tc extraction yield . . . 18
    3.4.2 ^{99}Mo and ^{99m}Tc retention . . . 18

4 Results & Discussion . . . 21
  4.1 Synthesis and characterization of molybdenum silicides . . . 21
    4.1.1 Sol-gel and carbothermic reduction method . . . 21
    4.1.2 Sol-gel and preoxidation method . . . 24
    4.1.3 Magnesiothermic reduction method . . . 27
  4.2 Chemical stability . . . 28
  4.3 Influence of media on ^{99}Mo and ^{99m}Tc extraction yield . . . 30
  4.4 Influence of media on ^{99}Mo and ^{99m}Tc retention in the material . . . 31

5 Conclusions . . . 33

6 Recommendations . . . 35

Bibliography . . . 37

Appendix A: Activity calculations . . . 45

Abbreviations

BET Brunauer-Emmett-Teller.

CA Carrier-Added.
CT Computed Tomography.

EDS Energy Dispersive Spectroscopy.

FTIR Fourier-Transform Infrared Spectroscopy.

HAC Hot Atom Chemistry.
HEU Highly Enriched Uranium.

ICDD International Centre for Diffraction Data.
ICP-MS Inductively Coupled Plasma Mass Spectrometry.
IT Isomeric Transition.

LEU Low Enriched Uranium.

PDF Powder Diffraction File.
PET Positron Emssion Tomography.

SA Specific Activity.
SEM Scanning Electron Microscopy.
SPECT Single Photon Emission Computed Tomography.

TEM Transmission Electron Microscopy.

XRD X-Ray Diffraction.

List of Figures

1.1 Simplified decay scheme of $^{99}\mathrm{Mo}$ and $^{99m}\mathrm{Tc}$ [6]. 1

2.1 (**a**) External view of a technetium generator produced by TechneLite. (**b**) Schematic diagram of the internal structure of a technetium generator [7][23]. 7
2.2 Radioactive decay of $^{99}\mathrm{Mo}$ and build-up of $^{99m}\mathrm{Tc}$ for multiple elutions of a technetium generator [38]. 8
2.3 Binary Mo-Si phase diagram [60]. 11
2.4 Schematic illustrations of the crystal structures of molybdenum silicides, (A) α-$MoSi_2$, (B) Mo_5Si_3, (C) Mo_3Si and (D) β-$MoSi_2$ [58]. 11
2.5 Scheme of the sol-gel method [75]. 11

4.1 Characterization of P1: **(a)** SEM image of EDS mapped section, **(b)** Mo mapping, **(c)** Si mapping, **(d)** O mapping. 21
4.2 TEM images of P1. 22
4.3 XRD pattern of P1 (top) and reference diffraction peaks for Mo and MoO_2 (bottom). 22
4.4 Characterization of P2: **(a)** SEM image of EDS elemental mapped section, **(b)** Mo mapping, **(c)** Si mapping, **(d)** O Mapping and **(e)** C Mapping. 23
4.5 XRD pattern of P2 (top) and reference diffraction peaks for MoO_2 and Mo_2C (bottom). 24
4.6 Characterization of commercial $MoSi_2$: **(a)** SEM image with EDS elemental mapped section highlighted, **(b)** Mo mapping, **(c)** Si mapping. 24
4.7 XRD pattern of commercial $MoSi_2$ material (top) and reference diffraction peaks for α-$MoSi_2$ (bottom). 25
4.8 Characterization of silica-coated $MoSi_2$: **(a)** SEM image with EDS elemental mapped section highlighted, **(b)** Mo mapping, **(c)** Si mapping, **(d)** O mapping. 25
4.9 IR spectra of commercial $MoSi_2$ and the silica-coated $MoSi_2$. 26
4.10 XRD pattern of SiO_2-coated $MoSi_2$ material (top) and reference diffraction peaks for α-$MoSi_2$ and Mo_5Si_3 (bottom). 26
4.11 **(a)** SEM image of the synthesized SiO_2 precursor. **(b)** XRD pattern of the synthesized SiO_2 precursor (top), SiO_2/MoO_3 intermediate (middle) and SiO_2/MoO_3 intermediate with increased Mo content (bottom) along with the reference diffraction peaks for MoO_3. 27
4.12 XRD pattern of the final product (top) and reference diffraction peaks for MoO_2, Si, $MgSiO_3$ and SiO_2 (bottom). 28
4.13 Stability of $MoSi_2$ in chemical environments. The graphs show the percentage of Mo washed off over the course of 10 sequential washes in MilliQ and MEK for **(a)** commercial $MoSi_2$ and **(b)** silica-coated $MoSi_2$. Percentage of Mo washed off after soaking for 0, 1, or 24 hrs in **(c)** MilliQ and **(d)** MEK for commercial and silica-coated $MoSi_2$ 29
4.14 Influence of media on extraction yield of $^{99}\mathrm{Mo}$ and $^{99m}\mathrm{Tc}$: Extraction after **(a)** 0, **(b)** 24 and **(c)** 48 hrs. 31
4.15 Influence of media on the retention of $^{99}\mathrm{Mo}$ and $^{99m}\mathrm{Tc}$ after **(a)** 0 and **(b)** 24 hrs. 32

A.1 Activity calculations immediately after irradiation. 45
A.2 Activity calculations after cooling. 46

List of Tables

2.1 Naturally occurring molybdenum isotopes [25]. 5
2.2 The main accelerator-based production routes for ^{99}Mo [4][13][29][30][31]. 6

3.1 Overview of chemicals. 15
3.2 List of all the instruments used. 16
3.3 List of all the apparatus used. 16
3.4 Neutron fluxes of the PB3 pneumatic system of the Hoger Onderwijs Reactor of the Reactor Institute Delft operating at 2.3 MW [89]. 18

4.1 Elemental surface composition of P1 acquired from EDS. 21
4.2 Weight percentage of Mo, Si and O elements in $SiO_{2/}MoO_3$ intermediates as determined by EDS elemental analyses. 27

1

Introduction

Cancer is one of the leading causes of death worldwide, accounting for nearly 10 million deaths in 2020 [1]. In recent decades, research in the field of preclinical molecular biology has led to significant advances in our understanding of cancer at the cellular level. However, the challenge of translating these findings into clinical applications persists, largely due to the lack of suitable tools for studying molecular events in patients. This gap has driven the development of molecular imaging, which enables non-invasive visualization, characterization, and monitoring of biological processes in cancer patients. Several imaging methods such as X-rays, ultrasound, computed tomography (CT), single photon emission computed tomography (SPECT) and positron emission tomography (PET) have been investigated to diagnose cancers and to evaluate the effectiveness of ongoing treatment procedures [2].

The advances in molecular imaging techniques have also required the development of innovative contrast agents and radionuclides, specifically designed to meet the unique diagnostic and therapeutic needs of each patient. Among these, technetium-99m ($^{99m}\mathrm{Tc}$) has become one of the most extensively utilized medical radionuclides, playing a crucial role in nuclear medicine diagnostics [3]. It is currently used in 80-85% of in-vivo nuclear medicine diagnostics, and its utilization is expected to increase by 3-8% each year [4]. $^{99m}\mathrm{Tc}$ is preferred for medical use due to its relatively short half-life ($t_{1/2}$ = 6.01 h), its unique chemistry that enables coordination with a wide range of organic compounds, and its emission of a single gamma photon with a low energy of 141 keV. This energy, is very suitable for penetrating tissues and is effectively detected by SPECT cameras from outside the body [5]. These advantages make $^{99m}\mathrm{Tc}$ highly effective for producing high-quality images of the target organs with minimal radiation exposure for the patient [4].

The majority of $^{99m}\mathrm{Tc}$ is produced by the decay of molybdenum-99 ($^{99}\mathrm{Mo}$) which has a half-life of 66 hours [3]. $^{99}\mathrm{Mo}$ decays to $^{99m}\mathrm{Tc}$ (87.5%) which then decays to $^{99g}\mathrm{Tc}$ through isomeric transition (IT). The other 12.5% of $^{99}\mathrm{Mo}$ decays directly to $^{99g}\mathrm{Tc}$, followed by the decay of $^{99g}\mathrm{Tc}$ ($t_{1/2}$ = $2.1 \cdot 10^5$ yr) to the stable $^{99}\mathrm{Ru}$ (Figure 1.1).

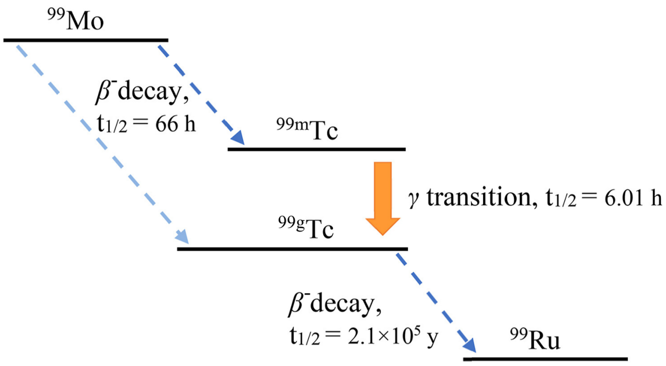

Figure 1.1: Simplified decay scheme of $^{99}\mathrm{Mo}$ and $^{99m}\mathrm{Tc}$ [6].

The current 'gold standard' procedure for generating $^{99}\mathrm{Mo}$ for medical isotope use includes neutron fission of $^{235}\mathrm{U}$ (i.e. $^{235}\mathrm{U}$(n,f)$^{99}\mathrm{Mo}$) in multipurpose research reactors [7]. Approximately 6.1% of the $^{235}\mathrm{U}$ fissions result in $^{99}\mathrm{Mo}$. This reaction has a larger cross-section (~35.6 barns for $^{99}\mathrm{Mo}$ production using thermal neutrons) than other methods of production.[1] Multipurpose research reactors are ideal for $^{99}\mathrm{Mo}$ production because of their ability to irradiate various targets at high neutron flux rates (usually around 10^{13}-10^{14} neutrons per square centimeter per second ($\mathrm{cm}^{-2} \cdot \mathrm{s}^{-1}$). Higher neutron fluxes mean more neutrons are present per unit area, leading to an increased likelihood of reactions occurring. The $^{235}\mathrm{U}$ nucleus absorbs a thermal neutron and initiates a fission process, producing two primary fission fragments. These fragments undergo further radioactive decay, ultimately yielding over 200 distinct radionuclides, including $^{99}\mathrm{Mo}$ [4]. Most fission-based $^{99}\mathrm{Mo}$ was produced using Highly Enriched Uranium (HEU) targets. However, because of the non-proliferation treaty, these targets are being converted to Low Enriched Uranium (LEU) targets to avoid the risk of nuclear weapons. This has a significant impact on the overall manufacturing costs and the quantity of nuclear waste, which increases by 200% [9].

Another reactor-based method for the production of $^{99}\mathrm{Mo}$ is through neutron activation of $^{98}\mathrm{Mo}$ (i.e., $^{98}\mathrm{Mo}(\mathrm{n}, \gamma)^{99}\mathrm{Mo}$). While this method has the potential to become a dominant reactor-based production route, it faces significant limitations due to the very small activation cross-section (0.13 barns for thermal neutrons), compared to the production cross-section of $^{235}\mathrm{U}$ fission (37 barns for $^{99}\mathrm{Mo}$ specifically) [10]. As a result, $^{99}\mathrm{Mo}$ produced through this method has a specific activity 2 to 4 times lower compared to $^{99}\mathrm{Mo}$ generated by neutron fission, since only a small fraction of the molybdenum is converted to $^{99}\mathrm{Mo}$ [11].[2] Although $^{98}\mathrm{Mo}$ neutron activation has remarkable potential for generating $^{99}\mathrm{Mo}$, its application in $^{99}\mathrm{Mo}/^{99m}\mathrm{Tc}$ generators using the existing alumina adsorbent is challenging. Finally, $^{99}\mathrm{Mo}$ can be produced through photofission of $^{100}\mathrm{Mo}$ (i.e. $^{100}\mathrm{Mo}(\gamma,\mathrm{n})^{99}\mathrm{Mo}$) where energetic photons are obtained by the irradiation of heavy targets with electron beams coming from linear accelerators. The cross-section for this reaction is similar to that of the $^{98}\mathrm{Mo}(\mathrm{n}, \gamma)^{99}\mathrm{Mo}$, being 0.16 barn [13].

Most commercial $^{99}\mathrm{Mo}/^{99m}\mathrm{Tc}$ generators are based on column chromatography, where $^{99}\mathrm{Mo}$ is adsorbed onto the acidified alumina in the form of molybdate ($\mathrm{MoO_4}^{2-}$) [7]. When $^{99}\mathrm{Mo}$ decays, it forms pertechnetate ($\mathrm{TcO_4}^{-}$), which binds less tightly to the alumina due to its lower charge. As saline solution (0.9% NaCl) passes through the column, an ion exchange process occurs between the chloride and pertechnetate ions, so that $^{99m}\mathrm{Tc}$ is eluded as sodium pertechnetate. However, because of the low adsorption capacity of alumina (only 20 mg Mo per g alumina [14]) combined with the low specific activity of neutron activated $^{99}\mathrm{Mo}$, a large amount of alumina is needed in order to adsorb a significant amount of $^{99}\mathrm{Mo}$ [15]. Studies are being conducted to address the issue of low specific activity products by exploring strategies such as enhancing Mo capacity through the use of nanomaterial adsorbents [15], or employing alternative separation processes such as solvent extraction and electrochemical approaches [16][17][18].

Another way of tackling this problem would be to develop a new generation of the $^{99}\mathrm{Mo}/^{99m}\mathrm{Tc}$ generator, where the material would be used as both the target material for neutron-activated $^{99}\mathrm{Mo}$ production and generator material for $^{99m}\mathrm{Tc}$ extraction. In doing so, the use of alumina adsorbents could be eliminated. To achieve the aforementioned dual functionality, several characteristics are required for the generator material. The material should have a high surface area, as this would minimize the amount of generated $^{99m}\mathrm{Tc}$ that remains 'trapped' in the material itself, thereby increasing $^{99m}\mathrm{Tc}$ extraction. Additionally, the material should be highly stable both in solution and during irradiation. Lastly, a high retention capacity for $^{99}\mathrm{Mo}$ is desirable to reduce impurities.

In this research, nanosized molybdenum silicides were investigated to be used as both target material for neutron-activated $^{99}\mathrm{Mo}$ production and generator material for $^{99m}\mathrm{Tc}$ extraction. Molybdenum silicides are known to be stable at high temperatures and in harsh conditions, and exhibit excellent oxidation resistance [19][20]. Nanostructured variants would provide a large surface to volume ratio, resulting in a high overall surface area [21]. Nanostructured materials of MoSi_x have not yet been neutron irradiated and analyzed for their extraction potentials of $^{99}\mathrm{Mo}$ and $^{99m}\mathrm{Tc}$, while also thinking about their reusability. This thesis aims to fill this research gap.

---

[1] The cross-section indicates the likelihood that a given nucleus will undergo a particular nuclear reaction. The probability term is measured in cm^2 and referred to as the reaction's cross-sectional area. The used unit is barn, where one barn equals 10^{-24} cm^2 [8].

[2] The specific activity is defined as the amount of radioactivity of a particular radionuclide per unit mass of that radionuclide, normally expressed as Bq/g [12].

The main objectives to be achieved during this research were:

1. Synthesize nanostructured molybdenum silicides
2. Study the chemical stability of this material in various solvents
3. Investigate the extraction potential of $^{99}\mathrm{Mo}$ and $^{99m}\mathrm{Tc}$ from this material
4. Study the retention of $^{99}\mathrm{Mo}$ and $^{99m}\mathrm{Tc}$ in the material

2

Theoretical Background

2.1. Production of ^{99}Mo

2.1.1. Fission-produced ^{99}Mo

$^{99}\mathrm{Mo}$ can be produced in a variety of ways, one of which is the fission of uranium targets in a reactor. The classification of these targets is based on the content of the fissile $^{235}\mathrm{U}$ radioisotope. These include natural uranium ($^{235}\mathrm{U}$ content ≈0.72%), LEU (0.72% < $^{235}\mathrm{U}$ < 20%), HEU (20% < $^{235}\mathrm{U}$ < 90%) and weapons-grade Enriched Uranium ($^{235}\mathrm{U}$ content > 90%) [4]. The majority of $^{99}\mathrm{Mo}$ for medical application is created through the fission of highly enriched uranium (HEU)-based targets, such as uranium-aluminum alloys. $^{99}\mathrm{Mo}$ can also be produced using low-enriched uranium (LEU) targets. However, it would only produce around 20% of the $^{99}\mathrm{Mo}$ yield compared to HEU for the same target mass [22]. In nuclear reactors, thermal energy and the fission neutron spectrum play a crucial role in the production of $^{99}\mathrm{Mo}$. The $^{235}\mathrm{U}$ nuclei absorb thermal neutrons to initiate fission. The fission of the $^{235}\mathrm{U}$ nucleus yields two to three lower mass nuclei known as fission fragments. In a nuclear reactor, uranium targets are exposed to a high neutron flux for five to seven days, resulting in the production of 6% $^{99}\mathrm{Mo}$ (production cross-section = 37 barns) [23]. The most common radioisotopes produced by fission include $^{99}\mathrm{Mo}$ (which decays to $^{99m}\mathrm{Tc}$), $^{131}\mathrm{I}$, and $^{133}\mathrm{Xe}$. The relevant fission reaction for this is:

$$^{235}\mathrm{U} + {}^{1}\mathrm{n}_{\mathrm{thermal}} \longrightarrow {}^{236}\mathrm{U} \longrightarrow {}^{99}\mathrm{Mo} + {}^{134}\mathrm{Sn} + 3\ {}^{1}\mathrm{n} \tag{2.1}$$

After irradiation, targets are transferred to processing facilities with hot cells to separate and purify $^{99}\mathrm{Mo}$ from other fission products. The carrier-free purified $^{99}\mathrm{Mo}$ solution is then loaded in the $^{99}\mathrm{Mo}/^{99m}\mathrm{Tc}$ generator. As $^{99}\mathrm{Mo}$ has a relatively short half-life ($t_{1/2}$ = 66 h), this must be done in as little time as possible, to minimize the decay of $^{99}\mathrm{Mo}$. The quantity of $^{99}\mathrm{Mo}$ generated is referred to as the ”six-day Curie”, the amount of $^{99}\mathrm{Mo}$ radioactivity that is still present 6 days after processing [24].

2.1.2. Neutron-capture-produced ^{99}Mo

Molybdenum has several naturally occurring isotopes, Table 2.1, amongst which $^{98}\mathrm{Mo}$ is the most abundant with 24.29%. Natural or enriched $^{98}\mathrm{Mo}$ targets can be activated by the capture of thermal neutrons in the thermal flux of conventional research reactors to yield $^{99}\mathrm{Mo}$ (eq. 2.2).

Table 2.1: Naturally occurring molybdenum isotopes [25].

Isotope	Abundance [%]	Thermal (n,γ) cross-section [barn]
$^{92}\mathrm{Mo}$	14.65	0.08
$^{94}\mathrm{Mo}$	9.19	0.34
$^{95}\mathrm{Mo}$	15.87	13.4
$^{96}\mathrm{Mo}$	16.67	0.55
$^{97}\mathrm{Mo}$	9.58	2.20
$^{98}\mathrm{Mo}$	24.29	0.13
$^{100}\mathrm{Mo}$	9.74	0.20

$$^{98}\mathrm{Mo} + {}^{1}\mathrm{n}_{\mathrm{thermal}} \longrightarrow {}^{99}\mathrm{Mo} + \gamma \tag{2.2}$$

Only a little amount of molybdenum is converted to $^{99}\mathrm{Mo}$, resulting in a Carrier-Added (CA) product with poor specific activity [26]. In other words, $^{99}\mathrm{Mo}$ activity is diluted by the presence of the inactive $^{98}\mathrm{Mo}$ target. Using enriched $^{98}\mathrm{Mo}$ target material improves the specific activity. The increase is proportional to the enrichment factor. Using enriched targets with a $^{98}\mathrm{Mo}$ content of ≥96% can increase the specific activity yield of $^{99}\mathrm{Mo}$ by four-fold [4]. One of the main factors that limit the specific activity is the small neutron capture cross-section of $^{98}\mathrm{Mo}$ targets (0.13 barns for thermal neutrons). If the irradiation is carried out in the epithermal energy zone, this number can be raised to 6.7 barns [27]. However, there are very few nuclear reactors which are sensitive specifically to neutrons in the epithermal energy region [28].

2.1.3. Accelerator-based ^{99}Mo production

$^{99}\mathrm{Mo}$ can also be produced using modern particle accelerators. This route would eliminate the need for HEU targets as well, and generate relatively low amounts of radioactive waste compared to the use of nuclear reactors [13]. The principle behind it is to accelerate charged particles, such as protons, deuterons, or electrons, in order to cause nuclear reactions in the material of interest. The accelerated particles can sometimes even interact with the target material to directly produce $^{99}\mathrm{Mo}$ or even $^{99m}\mathrm{Tc}$. An overview of the main production routes for accelerator-based $^{99}\mathrm{Mo}$ production can be found in Table 2.2.

Table 2.2: The main accelerator-based production routes for ^{99}Mo [4][13][29][30][31].

Facility	Accelerated particle	Incident particle	Target material	Nuclear reaction	Production cross-section [barn]
Electron accelerator	Electron	Photon	$^{nat.}\mathrm{U}$	$^{238}\mathrm{U}(\gamma,\mathrm{f})^{99}\mathrm{Mo}$	0.01
	Electron	Photon	$^{100}\mathrm{Mo}$	$^{100}\mathrm{Mo}(\gamma,\mathrm{n})^{99}\mathrm{Mo}$	0.16
Deuteron accelerator	Deuteron	Neutron	$^{100}\mathrm{Mo}$	$^{100}\mathrm{Mo}(\mathrm{n},2\mathrm{n})^{99}\mathrm{Mo}$	1.5
	Deuteron	Deuteron	$^{100}\mathrm{Mo}$	$^{100}\mathrm{Mo}(\mathrm{d},\mathrm{p}2\mathrm{n})^{99}\mathrm{Mo}$	0.30
Proton accelerator	Proton	Proton	$^{100}\mathrm{Mo}$	$^{100}\mathrm{Mo}(\mathrm{p},\mathrm{pn})^{99}\mathrm{Mo}$	0.15
				$^{100}\mathrm{Mo}(\mathrm{p},2\mathrm{p})^{99}\mathrm{Nb} \rightarrow {}^{99}\mathrm{Mo}$	0.16
	Proton	Proton	$^{232}\mathrm{Th}$	$^{232}\mathrm{Th}(\mathrm{p},\mathrm{f})^{99}\mathrm{Mo}$	0.03
α-particle accelerator	α-particle	α-particle	$^{96}\mathrm{Zr}$	$^{96}\mathrm{Zr}(\alpha,\mathrm{n})^{99}\mathrm{Mo}$	0.185

With electron accelerators, a high-intensity electron beam strikes a dense target material to generate Bremsstrahlung photons. These photons are then used to produce $^{99}\mathrm{Mo}$ through two different methods; a photon-induced fission reaction or photon-induced nuclear reaction. In the photon-induced fission reaction, high specific activity $^{99}\mathrm{Mo}$ can be obtained from the reaction $^{238}\mathrm{U}(\gamma,\mathrm{f})^{99}\mathrm{Mo}$. However, when comparing it to the neutron-initiated uranium fission method, the production output is around 3700 times lower as it has a much smaller reaction cross-section (0.16 barn) [13]. Following the photonuclear transmutation reaction, one can produce $^{99}\mathrm{Mo}$ according to the reaction $^{100}\mathrm{Mo}(\gamma,\mathrm{n})^{99}\mathrm{Mo}$.

Through bombardment of high energy neutrons on $^{100}\mathrm{Mo}$, $^{99}\mathrm{Mo}$ can be produced following the nuclear reaction $^{100}\mathrm{Mo}(\mathrm{n},2\mathrm{n})^{99}\mathrm{Mo}$. The cross-section for this reaction is about 1.5 barn, which is ten times higher than the cross-section for $^{98}\mathrm{Mo}(\mathrm{n},\gamma)^{99}\mathrm{Mo}$ in the thermal region. Furthermore, a high-intensity neutron flux of $\geq 10^{13}$ n/cm^{2}s and an irradiation period of more than 8 days are needed [32]. However, low specific activity $^{99}\mathrm{Mo}$ will be produced even when 100% enriched $^{100}\mathrm{Mo}$ is used, due to the inability to chemically separate the radionuclides [4].

Lastly, much research is done into other possibilities that make use of protons or deuterons for the production of $^{99}\mathrm{Mo}$. An example of this is the $^{100}\mathrm{Mo}(\mathrm{p},\mathrm{pn})^{99}\mathrm{Mo}$ reaction. However, this reaction has a low cross-section (0.15 barn) and yields low amounts of $^{99}\mathrm{Mo}$ [29]. In contrast, the reaction cross-section of $^{100}\mathrm{Mo}(\mathrm{d},\mathrm{p}2\mathrm{n})^{99}\mathrm{Mo}$ is twice as high (0.30 barn). However, irrespective of the higher cross-section, low specific activity $^{99}\mathrm{Mo}$ will be produced.

2.2. Production of ^{99m}Tc (^{99}Mo/^{99m}Tc generator)

A $^{99}\mathrm{Mo}/^{99m}\mathrm{Tc}$ generator, also known as 'technetium generator', is a device utilized for the extraction of technetium produced from $^{99}\mathrm{Mo}$. A typical generator includes a small alumina column, tubing, valves, and filters for technetium extraction, as well as lead shielding for radiation protection (see Figure 2.1). Alumina is used as it is known to have high radiation resistance and affinity for specific inorganic ions such as Mo [33].

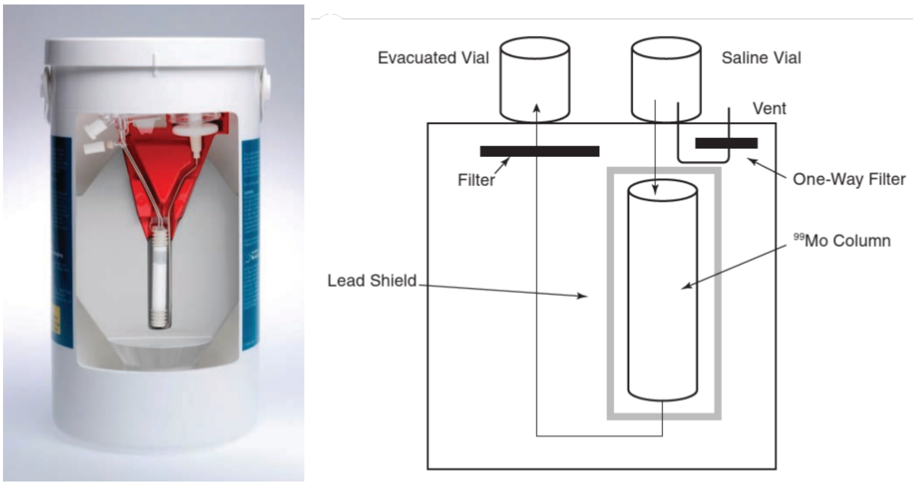

(a) (b)

Figure 2.1: (**a**) External view of a technetium generator produced by TechneLite. (**b**) Schematic diagram of the internal structure of a technetium generator [7][23].

In a typical technetium generator, $^{99}\mathrm{Mo}$ in the form of molybdate ($\mathrm{MoO_4}^{2-}$) is adsorbed onto the alumina column. $^{99}\mathrm{Mo}$ decays in the column, forming pertechnetate ($\mathrm{TcO_4}^{-}$). Because pertechnetate has a single charge, it is less tightly bound and has relatively limited interaction with the alumina. On passing saline (0.9% NaCl) solution through the column, an ion exchange process occurs between chloride and pertechnetate ions [34]. Over the generator's lifespan, the elution yields more than 80% of the theoretical amount of $^{99m}\mathrm{Tc}$ from the molybdenum $^{99}\mathrm{Mo}$ column [22]. There are two types of columns available: dry and wet column generators [33]. In dry generators, a set volume of saline is used for each elution. Saline is pulled through the column by a vacuum that is created by an evacuated vial attached to the outlet. In a wet generator, a saline reservoir is permanently attached to the inlet. During elution, saline is replaced from the reservoir, keeping the column full of liquid between elutions [35]. Generally, the wet generator has a higher $^{99m}\mathrm{Tc}$ elution efficiency (>85%) than the dry generator (>80%) [36]. However, it is challenging to load consistent levels of $^{99}\mathrm{Mo}$ during wet generator fabrication.

Due to the decay of $^{99}\mathrm{Mo}$ in the generator, a continuous in-growth of $^{99m}\mathrm{Tc}$ takes place. As the mother nuclide ($^{99}\mathrm{Mo}$) has a longer half-life than the short-lived daughter ($^{99m}\mathrm{Tc}$), a radioactive equilibrium is established. This state is called either a secular or transient equilibrium, dependent on the ratio of the half-lives. Secular equilibrium arises when the mother's half-life is much bigger than that of the daughter nuclide, $t_{1/2,mother} \gg t_{1/2,daughter}$. It is called transient equilibrium when $t_{1/2,mother} > t_{1/2,daughter}$, as is the case in the $^{99}\mathrm{Mo}/^{99m}\mathrm{Tc}$ generator system [37]. This transient equilibrium is reached after approximately four elapsed half-lives of $^{99m}\mathrm{Tc}$ [4].

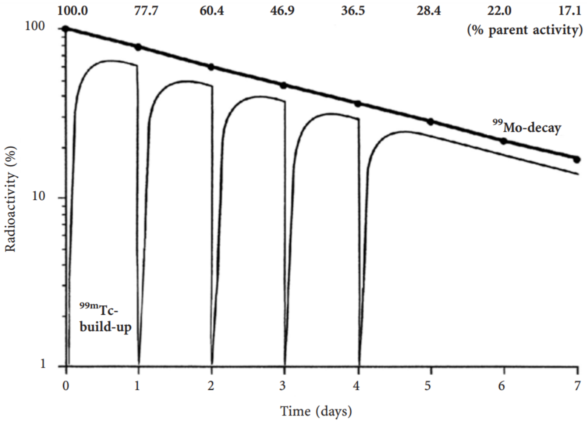

Figure 2.2: Radioactive decay of $^{99}\mathrm{Mo}$ and build-up of $^{99m}\mathrm{Tc}$ for multiple elutions of a technetium generator [38].

From Figure 2.2 it can be seen that during the $^{99m}\mathrm{Tc}$ ingrowth, its production is a lot faster than its decay. Once the equilibrium is established, the $^{99m}\mathrm{Tc}$ decay and growth rate are equal. Following elution, the generator repeats the process, with $^{99}\mathrm{Mo}$ decaying to produce fresh $^{99m}\mathrm{Tc}$. As a result, $^{99m}\mathrm{Tc}$ begins to be regenerated again. The correlation between the $^{99m}\mathrm{Tc}$ growth and the decay of $^{99}\mathrm{Mo}$ can be explained using the Bateman equations [4][39]:
The decay of $^{99}\mathrm{Mo}$ can be expressed as:

$$\frac{dN_1}{dt} = -\lambda_1 N_1 \tag{2.3}$$

$$N_1 = N_1^0 e^{-\lambda_1 t} \tag{2.4}$$

Where N_1 indicates the number of $^{99}\mathrm{Mo}$ atoms at time t in sec., N_1^0 is the amount of $^{99}\mathrm{Mo}$ atoms at t=0 s, and λ_1 is the decay constant of $^{99}\mathrm{Mo}$ in s^{-1}.

As the production of $^{99m}\mathrm{Tc}$ equals the decay of $^{99}\mathrm{Mo}$, the growth rate of $^{99m}\mathrm{Tc}$ can be written as:

$$\text{Growth rate} = \text{Production} - \text{Decay}$$

$$\frac{dN_2}{dt} = \lambda_1 N_1 - \lambda_2 N_2 = \lambda_1 N_1^0 e^{-\lambda_1 t} - \lambda_2 N_2 \tag{2.5}$$

$$N_2 = \frac{\lambda_1}{\lambda_2 - \lambda_1} N_1^0 (e^{-\lambda_1 t} - e^{-\lambda_2 t}) + N_2^0 e^{-\lambda_2 t} \tag{2.6}$$

Where N_2 is the amount of $^{99m}\mathrm{Tc}$ atoms at time t in sec., λ_2 is the decay constant of $^{99m}\mathrm{Tc}$ in s^{-1} and N_2^0 is the amount of $^{99m}\mathrm{Tc}$ atoms at t=0 s.

To obtain an equation in terms of activity, one can use the relation: A = λN. This results in:

$$A_1 = A_1^0 e^{-\lambda_1 t} \tag{2.7}$$

$$A_2 = \frac{\lambda_2}{\lambda_2 - \lambda_1} A_1^0 (e^{-\lambda_1 t} - e^{-\lambda_2 t}) + A_2^0 e^{-\lambda_2 t} \tag{2.8}$$

Here, A_1 is the activity of $^{99}\mathrm{Mo}$ in Bq at time t (s), A_1^0 is the activity of $^{99}\mathrm{Mo}$ in Bq at t=0 s, A_2 is the activity of $^{99m}\mathrm{Tc}$ in Bq at time t (s) and A_2^0 is the activity of $^{99m}\mathrm{Tc}$ in Bq at t=0 s.

Equation 2.8 can be used to quantify the eluted radioactivity.

2.3. Utilizing hot atom chemistry principles

Hot atom chemistry (HAC) is the study of chemical reactions involving thermal-energy and high energy atoms, molecules, ions, and radicals. Research includes the production of atoms and ions through photochemical processes, but mostly by nuclear processes [40]. In the latter, the chemical effects occur during nuclear transmutations, for example due to activation and radioactive decay. One of these activation methods is neutron activation. This involves irradiation of a nucleus with neutrons, after which a neutron is absorbed by the target nucleus. The compound nucleus that is formed is in a highly energetic state and emits gamma rays, a proton, a neutron, or an alpha particle to get rid of its excess energy [41]. It is also possible for a radionuclide to undergo various decay transmutations, such as α-, β^-- or β^+-decay, which is accompanied by the release of energy. This energy is distributed among the particles involved in the reaction and can be calculated by using the law of conservation of momentum. The recoil energy received by the daughter nuclide, is dependent on the energies of the emitted particles or photons [37]. These recoiling atoms are referred to as hot atoms because their kinetic energy is significantly greater than thermal equilibrium values [42]. As chemical binding energies between atoms range from 40 to 400 $\mathrm{kJmol^{-1}}$, or approximately 0.4 - 4 eV (1 eV $\approx$ 96.5 $\mathrm{kJmol^{-1}}$), this bond can be broken if the recoil energy is high enough, causing the produced radionuclide to be released from its chemical bond [3].

This principle can be utilized to produce radionuclides with higher specific activity by separating isotopic mother and daughter radionuclides, such as $^{98}\mathrm{Mo}$ and $^{99}\mathrm{Mo}$. The majority of Mo-atom bonds have an energy of around 5 eV so that prompt gamma energies of around 1000 keV are needed to acquire high enough recoil energies to break them [43][44]. Approximately 14.0 - 15.7% of the emitted prompt gammas have high enough energy to cause this [45]. Furthermore, when $^{99}\mathrm{Mo}$ decays to $^{99m}\mathrm{Tc}$ there is an 82% probability that the β^--particles have the maximum energy of 1.23 MeV [46]. This results in the daughter to have a recoil energy of approximately 12.5 eV. The recoiling atom will probably acquire part of this energy and therefore the bond may not be broken by recoiling effects. Despite this, the change of atomic number after β^--decay causes all electrons to be excited. The emission of electrons from the shell generates excitation energy and can break chemical bonds [37].

Wolterbeek, H.T., and Bode, P. have reported methods to increase the specific activity (SA) of neutron activated $^{99}\mathrm{Mo}$ using these principles [47]. Targets that have been used for this were molybdenum(0) hexacarbonyl [$\mathrm{Mo(CO)_6}$], molybdenum(VI) dioxodioxinate [$\mathrm{[C_4H_3(O)-NC_5H_3)]_2-MoO_2}$], molybdenum nanoparticles ($\sim$100 nm) and other molybdenum tricarbonyl compounds. The neutron irradiated targets were first dissolved in organic solvents, after which the $^{99}\mathrm{Mo}$ is extracted using an aqueous buffer solution. Doing so increased the specific activity of $^{99}\mathrm{Mo}$ by a factor of 1000, making the method comparable to that of the high SA $^{99}\mathrm{Mo}$ produced through fission of $^{235}\mathrm{U}$ [43]. However, these organic compounds were observed to be easily damaged by the gamma rays and neutrons during irradiation in the reactor [48].

Using inorganic targets could be a better alternative, as they are much more stable when exposed to the gamma rays [45]. A study on the chemical effects of the $^{98}\mathrm{Mo}(n,\gamma)^{99}\mathrm{Mo}$ reaction on molybdenum(II) chloride [$\mathrm{(Mo_6Cl_8)Cl_4}$] is one of these alternatives. It was concluded that this compound offers good prospects for practical applications, with yields of around 80% [49]. Another work by Ngo, M.C. investigated the use of $\mathrm{MoO_3}$ targets and concluded it to be a promising irradiation target in producing $^{99}\mathrm{Mo}/^{99m}\mathrm{Tc}$ by the (n,γ) method. When using water for radioisotope extraction, extraction yields of around 67% could be achieved [50]. Furthermore, a numerical study showed that 50% of activated $^{99}\mathrm{Mo}$ could recoil out when molybdenum disulfide nanoparticles are irradiated with neutrons [51]. However, comparing these different methods is difficult, as they all use different production methods.

It is good to note that none of the works presented addressed the extraction of $^{99m}\mathrm{Tc}$ using hot atom principles. These works were rather focused on the potential of utilizing (in)organic molybdenum compounds, as opposed to uranium-based $^{99}\mathrm{Mo}$ production, to produce high specific activity $^{99}\mathrm{Mo}$ that is compatible with existing technetium generators.

2.4. Fundamentally different ^{99}Mo/^{99m}Tc generator

As described in the previous section, the specific activity of $^{99}\mathrm{Mo}$ can be improved through the use of hot atom chemistry. The high SA $^{99}\mathrm{Mo}$ can then be loaded into conventional technetium generators to produce the desired $^{99m}\mathrm{Tc}$. However, the disadvantage of this method is its difficulty to achieve both high yields and significant enrichment factors.[3] A more efficient approach could be to retain $^{99}\mathrm{Mo}$ within the material, allowing it to decay into $^{99m}\mathrm{Tc}$. During decay, there would be additional opportunities for bond rupture to occur through chemical effects such as recoil energy from radioactive decay or radiolysis, potentially improving the extraction efficiency of $^{99m}\mathrm{Tc}$.

In practice, such a system might pave the way for the development of an entirely new type of generator that is not limited by the physical limits of alumina-based designs. As hot atom chemistry only affects radioactive atoms, any unreacted or stable molybdenum will retain in the material. $^{99m}\mathrm{Tc}$ can be directly extracted from the material, eliminating the need for an alumina adsorbent for separation. This provides new opportunities for more compact and efficient generators. To extract $^{99m}\mathrm{Tc}$, liquid-extraction techniques can be utilized due to its easy usability, their widespread implementation in similar research and acceptance in hospitals [50][53][54].

For this idea to work, the target material must meet certain key criteria. First and foremost, the material must be highly stable, capable of withstanding high temperatures and irradiation damage while maintaining structural integrity, ensuring that it can be reused after each irradiation cycle [55]. Additionally, materials with high surface areas should be selected to minimize the amount of $^{99m}\mathrm{Tc}$ that remains ”trapped” within the material, thus increasing the overall yield of the process. Once all the $^{99}\mathrm{Mo}$ has decayed into $^{99m}\mathrm{Tc}$, the target material can then be sent back to a reactor facility and be re-irradiated, allowing for a continuous cycle of $^{99m}\mathrm{Tc}$ production until all molybdenum has been utilized. This process could significantly improve both the sustainability and efficiency of medical isotope generation, decreasing the dependency on traditional generator systems and aged reactors.

2.5. Molybdenum silicides

Molybdenum silicides belong to the group of transition metal silicides. This class of compounds exhibit both metallic and ceramic properties, with the advantages of good electrical conductivity, high temperature resistance and oxidation corrosion resistance [56]. The Mo-Si binary phase diagram (Figure 2.3) shows that three stoichiometries have been found for molybdenum-silicon; Mo_3Si, Mo_5Si_3 and $MoSi_2$. Both Mo_3Si and $MoSi_2$ are stoichiometric compounds, whereas Mo_5Si_3 has a homogeneity range of 3 at% Si.[4]

The crystal structure of these compounds vary (Figure 2.4). Mo_3Si adopts a cubic A15 structure with 8 atoms in the unit cell, consisting of 6 molybdenum and 2 silicon atoms [58]. Mo_5Si_3 possesses a body-centered tetragonal structure with a larger unit cell, consisting of 32 atoms - 20 molybdenum and 12 silicon atoms. $MoSi_2$ features two phases: the $C11_b$ (α-phase) and the C40 (β-phase). The $C11_b$ structure has I4/mmm symmetry, with sixfold-coordinated hexagonal $MoSi_2$ layers stacked in an ABAB sequence along the [110] direction [59]. In comparison, the C40 structure exhibits P6222 symmetry, consisting of identical hexagonal layers of $MoSi_2$ stacked in an ABCABC sequence. While the $C11_b$ structure is stable up to the melting point of $MoSi_2$, recent studies have shown that the previously reported high-temperature C40 phase is likely stabilized by the presence of impurities [19].

---

[3] The enrichment factor is defined as the ratio by which the specific activity increases due to the Szilard-Chalmers method, compared to when no separation is performed under identical irradiation conditions [52].

[4] A homogeneity range denotes the boundaries within which the quantity ratio of the individual metals may vary [57].

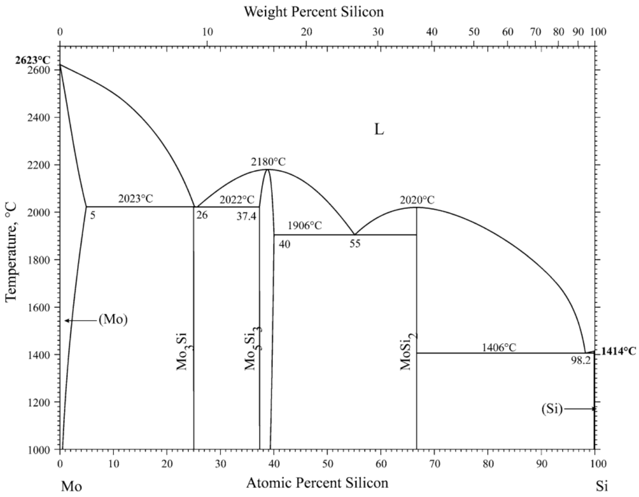

Figure 2.3: Binary Mo-Si phase diagram [60].

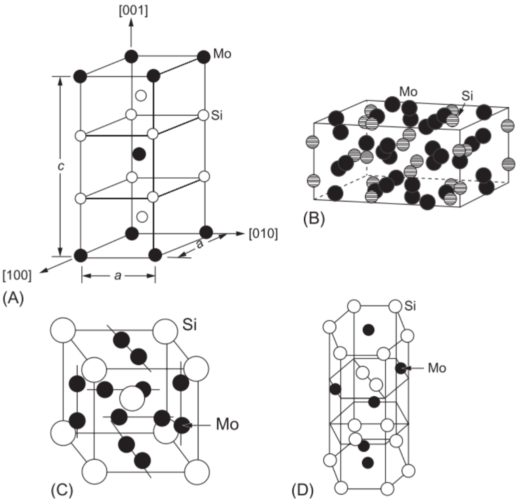

Figure 2.4: Schematic illustrations of the crystal structures of molybdenum silicides, (A) α-$MoSi_2$, (B) Mo_5Si_3, (C) Mo_3Si and (D) β-$MoSi_2$ [58].

Of these stoichiometric compounds, $MoSi_2$ has attracted most research interest due to its high melting point (2030 °C), rather low density, high electrical conductivity and high oxidation resistance in the range of 700 - 1700 °C [20][58]. They have important applications in the microelectronics industry as they are used in integrated circuits for Schottky barriers, Ohmic contacts and low-resistance gates [59]. Beside these applications, they are also used for heating components and structural parts at high temperatures. Yet, applications are limited due to low toughness at room temperature, low strength at high temperatures, and poor oxidation resistance at relatively low temperatures (500 - 600 °C) [61]. Reducing the grain sizes below nanometers, can optimize the characteristics of $MoSi_2$. Nanocrystalline $MoSi_2$ has superior fracture toughness and flexural strength compared to coarse-grained materials [20].

Various methods have been investigated for the synthesis of $MoSi_2$ nanoparticles. These include self-propagating high-temperature synthesis [62][63][64], shock wave synthesis [65][66], mechanical alloying [67][68][69], sonochemical synthesis [70] and chemical vapor deposition methods [71]. However, none of these methods are perfect. The sonochemical method induces a substantial amount of carbonaceous contaminants from the solvent. Mechanical alloying introduces iron, nitride, and oxide impurities and the obtained product has larger micro-sized particles with a nanocrystalline structure [20]. When following self-propagating high-temperature synthesis, pores and cracks often form due to the reaction's intense nature, thermal shock, and steep thermal gradients [19], and shock wave synthesis result in fully reacted, partially reacted and unreacted regions [66].

On the other hand, sol-gel processes have been studied as established methods for the preparation of nanomaterials [72]. An overview of this method is shown in Figure 2.5. Through modification of these processes, it should be possible to synthesize molybdenum silicides with dimensions confined to the nanometer scale [20][73]. Additionally, molybdenum silicide nanomaterials have been successfully synthesized through magnesiothermic reduction methods [74].

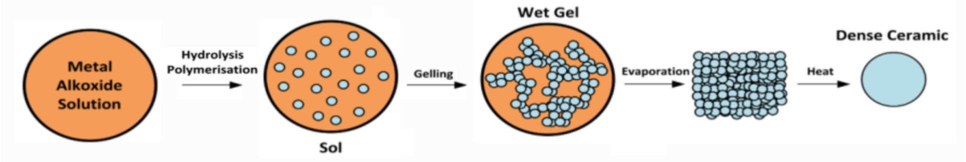

Figure 2.5: Scheme of the sol-gel method [75].

2.6. Measurement techniques

2.6.1. Brunauer-Emmett-Teller (BET) analysis

Brunauer-Emmett-Teller (BET) analysis is used to derive the specific surface area (m^2/g) of the samples. The fundament of BET theory is the adsorption of a gas on the material's surface [76]. This phenomenon originates from van der Waals forces generated by an adsorbate film composed of atoms, ions, or molecules on the surface of a substance that adsorbs these particles. Adsorption can occur either physically or chemically. Chemical adsorption results from a chemical reaction between the solid and the adsorbate (gas), whereas physical adsorption is related to van der Waals forces. The quantity of adsorbed gas on the adsorbent material can be attributed to its surface area. Several parameters influence this process, including temperature, pressure, and material properties.

2.6.2. Fourier-Transform Infrared Spectroscopy (FTIR)

Fourier-Transform Infrared Spectroscopy (FTIR) is used to study the functional groups of the samples by measuring the intensity and wavelength of the absorption of IR radiation [77]. It is based on the shift in a molecule's dipole moment, using the concept of vibrating molecular bonds and the subsequent absorption wavelengths, which are determined by the atoms involved and the strength of intermolecular interactions [78]. In an IR spectrum, the % transmittance (or absorbance) is plotted on the y-axis, whereas the x-axis represents the wavenumber (cm^{-1}). The peaks in the spectrum are specific to the frequencies of IR radiation that different types of bonds absorb [79].

2.6.3. Germanium gamma counter

The germanium gamma counter is a device used to measure the gamma spectrum of radioactive samples to assess their (relative) activity. This instrument consists of a semiconductor radiation detector assembly and signal processing devices that are connected to a pulse height analyzer and computer [80]. The detector is made of a semiconductor crystal that sits in between two conductor electrodes. Between the electrodes, a potential difference is created so that an electric field is produced in the semiconductor. When a γ-ray photon reaches the semiconductor, it generates free charge carriers in the crystal that are proportional to the energy lost by the photon. The electric field causes charge migration, which results in an induced current pulse in the external circuit. The integrated current pulse is proportional to the energy lost by γ-ray photons. These pulses are then sent to a multichannel pulse-height analyzer, which sorts and stores them, producing a pulse-height graph. The counts for a particular nuclide can be obtained by integrating over a certain region of interest.

2.6.4. Inductively Coupled Plasma Mass Spectrometry (ICP-MS)

Inductively Coupled Plasma Mass Spectrometry (ICP-MS) is an analytical technique that can be used to measure elements in small concentrations [81][82]. In the sample introduction system, liquid samples are nebulized to create a fine aerosol that is then transferred to the argon plasma. The sample is then atomized and ionized by the plasma, producing ions that are subsequently extracted through the interface region and into an electrostatic lens set known as the ion optics. The ion beam is directed and focused into the quadrupole mass analyzer by the ion optics. Ions are separated by the mass analyzer based on their mass-charge ratio (m/z), and the detector measures these ions. An internal standard is usually used to correct for deviations in instrument operating conditions or sample specific matrix effects that could alter the analyte signal. Every sample has the same amount of internal standard added to it. The analyte to internal standard signal ratio is then used to calculate the results.

2.6.5. Scanning Electron Microscopy (SEM)

Scanning electron microscopy (SEM) is a method used to visualize the size and morphology of samples. A highly focused electron beam is directed from an electron gun situated at the top of the sample [83]. When an electron beam meets the sample, it emits X-rays and three types of electrons: back scattered (primary), secondary, and Auger electrons. SEM uses both primary (back scattered) and secondary electrons. The identification of elemental compositions is achieved through the utilization of the characteristic X-rays, employing a technique known as Energy Dispersive Spectroscopy (EDS). This technique provides an overall mapping of the sample by analyzing near-surface elements and estimating the elemental proportion at different positions.

2.6.6. Transmission Electron Microscopy (TEM)

Transmission Electron Microscopy (TEM) is a technique that can be used to obtain chemical and crystallographic characterization of samples with high spatial resolution [84]. When the electron beam interacts with the material, diffraction occurs. The intensity of this diffraction is dependent on the plane's orientation with respect to the electron beam. At certain angles, the beam is strongly diffracted, whereas it is transmitted at other angles. The specimen's holders can be tilted in order to achieve a specific diffraction condition. Placing the aperture in such a way that the deflected electrons are blocked, allows unscattered electrons to pass through, resulting in a contrast image known as the light field. Using the deflected electrons to create an image is also possible, resulting in a ”dark field image” [83].

2.6.7. X-Ray Diffraction (XRD)

X-ray diffraction is a method that is used to characterize the crystal structure of powder samples based on the diffraction of X-rays. The principle of XRD can be understood from Bragg's law of diffraction [85]:

$$n\lambda = 2d \times \sin\theta \tag{2.9}$$

Here the n stands for the diffraction order, λ is the wavelength of the incoming x-ray beam in m, d stands for the ‘grating constant’ also called the lattice spacing in m and θ is the angle between the ray of incident on the plane surface and the sample.

X-Ray diffraction patterns are created by interference of a beam of X-rays scattered at specific angles. The distribution of atoms within the lattice determines peak intensities [86]. This information is converted into a graph where the intensity of a peak is plotted against the angle of diffraction 2θ. The samples are subjected to XRD analysis to provide insight into their structural characteristics, including phase identification.

3

Materials & Methods

This chapter gives an overview of the materials used and explains the experimental process.

3.1. Materials & Devices

The chemicals used can be found in Table 3.1.

Table 3.1: Overview of chemicals.

Chemical	Chemical Formula	Purity	Supplier
Ammonia	NH_3 (aq)	28-30%	Merck Sigma
Ammonium heptamolybdate	$(NH_4)_6Mo_7O_{24} \cdot 4\,H_2O$	>99%	Merck Sigma
Ethanol	C_2H_6O	≥99.9%	Sigma-Aldrich
Hydrochloric acid	HCl	≥30%	Merck Sigma
Hydrofluoric acid	HF	≥48%	VWR
Isopropanol	C_3H_8O	≥99.8%	Honeywell
Magnesium	Mg	-	J.T. Baker
Methyl ethyl ketone	C_4H_8O	≥99%	Sigma-Aldrich
MilliQ	H_2O	-	Ultrapure water system, Advantage A10, Merck
Molybdenum disilicide	$MoSi_2$	99.5% Mo 61 wt% min.	Alfa Aesar
Silicon dioxide, microspheres 30 nm	SiO_2	99.9%	Shanghai Macklin Biochemical Co., Ltd.
Silicon dioxide, 50 wt% in H_2O	SiO_2	50 wt%	Alfa Aesar
Sucrose	$C_{12}H_{22}O_{11}$	-	J. T. Baker
Tetraethyl orthosilicate	$Si(OC_2H_5)_4$	99.0%	Sigma-Aldrich

The instruments and apparatuses used can be found in Table 3.2 and Table 3.3, respectively.

Table 3.2: List of all the instruments used.

Instrument	Type	Supplier
Balance	Semi-Micro Analytical balance GR-202	A&D instruments LTD
FTIR spectrometer	Nicolet iS50 FTIR	Thermo Scientific
HPGe detector	Ge(Li) detector model IG22	Princeton Gamma-Tech
ICP-MS	NexION 2000 ICP-MS Single quat	PerkinElmer
Scanning Electron Microscope (SEM) with X-ray spectroscopy	JSM-IT100	JEOL
Surface Area and Porosity analyzer	TriStar II 3020	Micromimetics
Transmission Electron Microscope (TEM)	JEM-1400 Plus TEM	JEOL
X-ray Powder Diffractometer	X'Pert Pro MPD TTK-450	PANalytical

Table 3.3: List of all the apparatus used.

Apparatus	Type
Centrifuge (15-50mL)	Mega Star 600R centrifuge
Centrifuge (Eppendorf)	Micro Star 17R microcentrifuge
Furnace	Carbolite TF tube furnace
Magnetic stirrer	Heater and magnetic stirrer Arec
Oven	Carbolite HTCR oven
Oven	Ventricell ecol line
Pipette (2-20 µL)	Biohit
Pipette (1 mL)	Gilson
Pipette (5 mL)	Gilson
Sonic bath	5800 Ultrasonic cleaner
Vacuum oven	Vacutherm

3.2. Material synthesis

In this study, three distinct methodologies were employed to synthesize molybdenum silicides. These methods are outlined below.

Method 1: Sol–gel and carbothermic reduction method

The first synthesis is based on the method by J. Xu, et al. [87]. 3 g of ammonium heptamolybdate tetrahydrate [$(NH_4)_6Mo_7O_{24}\cdot 4\,H_2O$] and 3.5 g of sucrose were dissolved in 32 mL of deionized (DI) water in a glass beaker and stirred for 15 minutes using a magnetic stirrer. After this, 5.5 mL of concentrated hydrochloric acid (10 M) was added while stirring continuously for 1 hour until the solution turned dark blue. Subsequently, 7.6 mL of tetraethyl orthosilicate (TEOS) and 10 mL isopropanol were added to the mixture, which was stirred for another hour at 50 °C. The resulting solution was left to dry at room temperature for 18 hours. Afterward, 6 mL of ammonia solution was added, and the resulting wet gel was dried under vacuum at 110 °C for 5 hours. The dried gel was cooled and transferred into an alumina crucible and put in the sintering furnace under an argon atmosphere. The gel was heated at 200 °C for 2 hours before being ramped up at 10 °C/min to 1100 °C and sintered for another 2 hours. Finally, the product was rinsed with a 5% hydrofluoric acid (HF) solution, MilliQ and ethanol, and dried at 50 °C in a vacuum oven overnight yielding the final product.

This synthesis was repeated, resulting in two separate batches, from this point onward referred to as P1 and P2.

Method 2: Sol-gel preoxidation method

The second synthesis followed the research of L. Guo, et al. [73]. 5 g of molybdenum disilicide ($MoSi_2$) was dispersed in 50 mL of ethanol and treated with ultrasonic dispersion for 30 minutes to ensure homogeneous distribution. Subsequently, 1.43 mL of silicon dioxide solution (50 wt% in H_2O) was added to the mixture dropwise. The suspension was stirred at 500 rpm for 4 h using a magnetic stirrer to maintain a well-dispersed solution and prevent the sedimentation of $MoSi_2$ particles. The resulting suspension was centrifuged at 3,500 rpm for 30 min to collect the powder, followed by drying in an oven at 105 °C for 2 h and then at 220 °C for an additional 2 h. Afterward, the sample was ground with a mortar and pestle to break the agglomerates and preoxidized by heating to 800 °C in air for 2 h in the furnace to obtain the final product.

Method 3: Magnesiothermic reduction method

The third synthesis was done according to research of L. Wu, et al. [74]. First, SiO_2 nanoparticles were synthesized according to the modified Stöber method. 18 mL of ammonia solution ($NH_3 \cdot H_2O$), 32 mL of ethanol and 50 mL of MilliQ were mixed and stirred at room temperature to obtain a homogeneous solution, labeled as "solution A". A second solution, solution B, was obtained by adding 9 mL of tetraethyl orthosilicate (TEOS) to 91 mL of ethanol. Subsequently, solution B was immediately added to solution A. After continuously stirring for 2 h, the SiO_2 nanoparticles were obtained by centrifugation at 9,000 rpm for 10 min, washing it with MilliQ and drying at 80 °C.
To synthesize the Si/$MoSi_2$ nanocomposites, 0.1 g of ammonium heptamolybdate tetrahydrate [$(NH_4)_6Mo_7O_{24} \cdot 4\,H_2O$] and 1 g of SiO_2 were dissolved in 50 mL MilliQ and stirred for 30 min to obtain a homogeneously distributed solution. The suspension was then stirred at 100 °C to remove water, and the obtained powder was calcined at 400 °C for 2 h, resulting in SiO_2/MoO_3 powder. To increase the molybdenum content, the synthesis was also conducted using 1.46 g of ammonium heptamolybdate. After this, SiO_2/MoO_3 was mixed with magnesium powder with a mass ratio of 1:1 and put in a furnace under argon atmosphere. The furnace was first heated to 400 °C at a rate of 5 °C/min and then to 700 °C with a ramp rate of 2 °C/min where it was kept for 6 h. The Si/$MoSi_2$ nanocomposite was obtained after immersing the obtained powder in 2 M HCl solution for 6 h, then washing it with MilliQ and vacuum drying at 60 °C.

3.2.1. Characterization

The particle size and morphologies of the compounds were analyzed using Scanning Electron Microscopy (SEM). A thin layer of sample was put on double-sided carbon tape and analyzed at 15 keV acceleration voltage. The elemental distribution and purity of the materials were qualitatively and quantitatively determined by Energy Dispersive Spectroscopy (EDS) through detectors attached to the SEM. Transmission Electron Microscopy (TEM) was used to analyze particle sizes and check for particle agglomeration. This was done at an acceleration voltage of 120 keV. Generally, 2 mg of sample was dispersed in 0.5 mL of MilliQ and sonicated to achieve a homogeneous suspension. An aliquot of this suspension was drop-cast onto a TEM grid (200 mesh copper). These were air-dried at room-temperature before being analyzed by TEM.

Phase identification and degree of crystallinity were determined from XRD patterns on a diffractometer using a Cu-K_α radiation source. The data were collected in a scanning region between 2θ = 5–90° at a voltage of 45 kV and a current of 40 mA (scan rate = 1.55 °/min). The samples were analyzed using an open sample holder. Acquired data was analyzed using the software Match! and compared to the Powder Diffraction Files (PDF) from the International Centre for Diffraction Data (ICDD) [88].

To study the surface chemical groups of certain materials, Fourier-Transform Infrared Spectroscopy (FTIR) analysis was performed. This was done using solid samples.

Nitrogen adsorption-desorption isotherm measurements were done at 77 K on ~100 mg of sample. The specific surface area was determined from Brunauer-Emmett-Teller (BET) analysis. Before measurements, the samples were degassed at 120 °C for 15 hr to remove adsorbed species.

3.3. Stability tests

The stability of the commercial and silica coated $MoSi_2$ was tested in MilliQ and methyl ethyl ketone (MEK). These experiments were done in triplicate. For experiments where the material was washed, 10 mg of material was dispersed in 500 µL media and sonicated for 2 min. The samples were transferred into centrifugal filters and centrifuged (13,000 rpm, 1 min). The filtrate was then transferred into a separate tube for Mo breakthrough analysis, and 500 µL fresh media was added to the centrifugal filters. This was repeated 9 times, so that the samples were washed for a total of 10 times by either MilliQ or MEK. The samples containing MEK were dried at 80 °C overnight so that all MEK was evaporated, after which 500 µL of 1% HCl was added into each tube.

After this, the stability of these samples over time was tested. This was done by again adding 500 µL of fresh media to the centrifugal filters after the washes and leaving them for 1 and 24 hrs to determine the Mo breakthrough over time. Again, the filtrate was taken after soaking and fresh media was added to soak for the next time period.

Aliquots of 25 µL for MilliQ samples and 200 µL for MEK samples were diluted to 5 mL with 1% HCl prior to ICP-MS measurements. The percentage of molybdenum washed off from the materials was determined based on the measured concentration of $^{98}\mathrm{Mo}$.

3.4. Irradiation experiments

The irradiation experiments were performed at the Hoger Onderwijs Reactor of the Reactor Institute Delft BP3 pneumatic irradiation facility. The estimated neutron fluxes in the BP3 facility for a reactor power of 2.3 MW can be found in Table 3.4.

Table 3.4: Neutron fluxes of the PB3 pneumatic system of the Hoger Onderwijs Reactor of the Reactor Institute Delft operating at 2.3 MW [89].

Neutron type	Neutron flux
Thermal neutrons (0–0.5 eV)	$4.5{\cdot}10^{12}$ cm^{-2}s^{-1}
Epithermal neutrons (0.5 eV-1 keV)	$8.7{\cdot}10^{10}$ cm^{-2}s^{-1}
Fast neutrons (1 keV-20 MeV)	$3.3{\cdot}10^{11}$ cm^{-2}s^{-1}

All experiments were done in triplicate. The uncertainties were reported as one standard deviation from the mean in absolute terms. All samples were counted by the germanium gamma counter and the (relative) activity of $^{99m}\mathrm{Tc}$ and $^{99}\mathrm{Mo}$ were assessed by measuring the specific gamma rays emitted by the radioisotopes (140 keV and 740 keV, respectively) [90].

3.4.1. ^{99}Mo and ^{99m}Tc extraction yield

To measure the extraction yield of $^{99}\mathrm{Mo}$ and $^{99m}\mathrm{Tc}$, 35-40 mg of material was irradiated for 10 hours followed by a cooling period of 10 hours to allow the decay of short-lived activation products. After cooling, the capsules containing the irradiated materials were transferred to vials containing 3.5 mL of either MilliQ or methyl ethyl ketone (MEK). The solution was sonicated for 15 min and further homogenized by repeated pipetting. Subsequently, 500 µL of sample was transferred to a centrifugal filter and centrifuged (13,000 rpm, 1 min). The filtrate was collected and an additional 500 µL aliquot was centrifuged. These two filtrates combined were the first wash. Afterward, 500 µL of fresh media was added to the centrifugal filter and centrifuged. The filtrate was collected and this was done for an additional 3 times so that the material was washed for a total of 5 times. The obtained samples were then analyzed using a germanium gamma counter to assess the $^{99}\mathrm{Mo}$ breakthrough and $^{99m}\mathrm{Tc}$ extraction.

To determine whether additional extraction of $^{99m}\mathrm{Tc}$ or $^{99}\mathrm{Mo}$ could be achieved over a longer time period, 500 µL of fresh media was added to the centrifugal filter containing the irradiated material and allowed to soak for 24 hours. Following this soaking period, the filter was centrifuged, and the filtrate was collected. The collected filtrate was subsequently analyzed for $^{99}\mathrm{Mo}$ breakthrough and $^{99m}\mathrm{Tc}$ extraction.

3.4.2. ^{99}Mo and ^{99m}Tc retention

Obtaining stock solution

To prepare the stock solution for the retention determination of $^{99}\mathrm{Mo}$ and $^{99m}\mathrm{Tc}$ in the materials, the same initial procedure as in the extraction yield experiments was followed: approximately 35-40 mg of material was irradiated for 10 hours, followed by an 8-hour cooling period. The irradiated material was suspended into 2 mL of media (MilliQ or MEK), sonicated for 15 min and further homogenized by repeated pipetting. After this, 500 µL aliquots of the sample were sequentially filtered as described in the extraction method, with the filtrates combined to form the stock solution.

Retention experiments

To test the retention of $^{99}\mathrm{Mo}$ and $^{99m}\mathrm{Tc}$ in the synthesized compounds, approximately 10 mg of non-irradiated material was weighted and transferred to a centrifugal filter. A 500 µL aliquot of the stock solution was first analyzed for $^{99m}\mathrm{Tc}$ and $^{99}\mathrm{Mo}$ using gamma counting, and then added to the centrifugal filter. The filter was centrifuged (13,000 rpm, 1 min) and the filtrate was collected. Next, 500 µL of fresh media (either MilliQ or MEK) was added to the centrifugal filter, which was centrifuged under the same conditions. The second filtrate was collected in a separate vial. Both filtrate samples and the residue were subsequently analyzed to assess the retention of $^{99}\mathrm{Mo}$ and $^{99m}\mathrm{Tc}$.

To test the effect of extended soaking, the previously obtained filtrate was placed back in the centrifugal filter and allowed to soak for 24 hours. Following this period, the filter was centrifuged, and the filtrate was collected. The collected filtrate was then analyzed using the gamma counter.

4

Results & Discussion

In this chapter, the results of the experimental method are presented and discussed.

4.1. Synthesis and characterization of molybdenum silicides

4.1.1. Sol-gel and carbothermic reduction method

Characterization of P1

Figure 4.1 depicts the SEM images of P1 along its surface elemental composition (Table 4.1). The SEM images reveal that the particle sizes are in the micrometer range. However, TEM images (Figure 4.2) indicate the aggregation of nanosized particles. Elemental mapping via EDS demonstrated a homogeneous distribution of elements, though a significant amount of oxygen was also detected (Table 4.1). Further characterization using XRD was performed to identify the phases present in the sample.

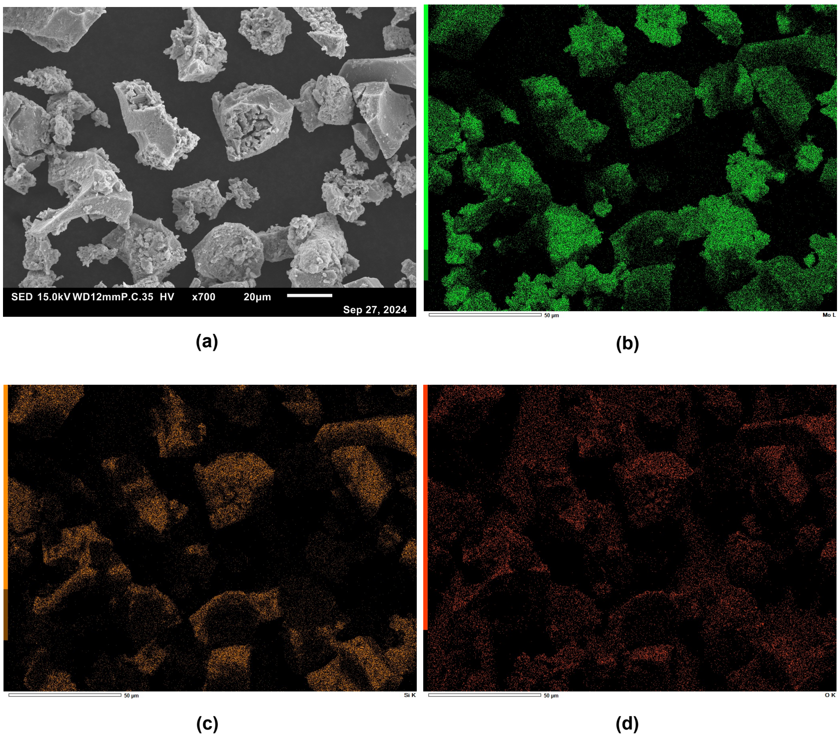

Figure 4.1: Characterization of P1: **(a)** SEM image of EDS mapped section, **(b)** Mo mapping, **(c)** Si mapping, **(d)** O mapping.

Element	Wt.%	At.%
Mo	57.4	19.9
Si	9.5	11.2
O	33.2	68.9

Table 4.1: Elemental surface composition of P1 acquired from EDS.

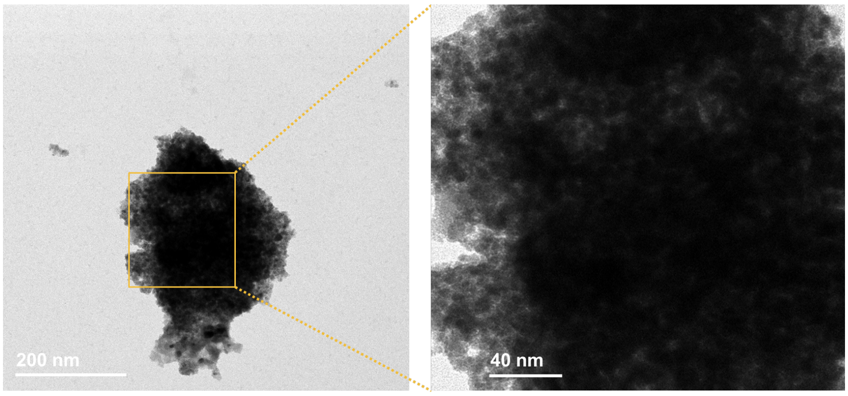

Figure 4.2: TEM images of P1.

To identify the phases in P1, XRD analysis was performed (Figure 4.3). The diffraction peaks, compared to reference patterns, revealed no formation of molybdenum silicides. Instead, the products included elemental molybdenum (PDF: 96-151-2522) and molybdenum dioxide (PDF: 96-154-8821). The broadening of the peaks, suggests the material having low crystallinity.

According to the original synthesis method, the process begins with the formation of silica and molybdenum trioxide. Subsequently, molybdenum trioxide undergoes carbothermic reduction to produce elemental molybdenum (Equation 4.1), which then reacts with silica to form molybdenum silicides (Equation 4.2).

$$\mathrm{MoO_3 + 3\,C \longrightarrow Mo + 3\,CO} \tag{4.1}$$

$$\mathrm{Mo + 2\,SiO_2 + 4\,C \longrightarrow MoSi_2 + 4\,CO} \tag{4.2}$$

Elemental mapping confirmed the presence of silicon and oxygen, suggesting that silica had formed. However, the absence of silica peaks in the XRD pattern indicates that the silica is amorphous and cannot confirm its presence. The peaks corresponding to elemental molybdenum confirm successful carbothermic reduction, though the presence of MoO_2 peaks suggest incomplete reduction of molybdenum trioxide or reoxidation of molybdenum.

This incomplete reduction could be attributed to issues with the tube furnace, which showed cracks in the tube after some uses. It is possible that oxygen leaked into the system during heating, leading to simultaneous oxidation and reduction reactions. The final synthesis step involves washing the sample with 5% HF to dissolve produced oxides and purify the product. However, as MoO_2 is insoluble in HF [91], any residual MoO_2 would remain in the final product.

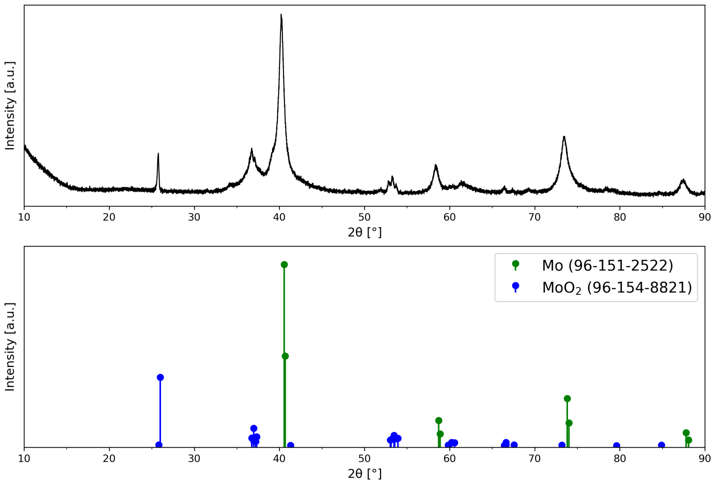

Figure 4.3: XRD pattern of P1 (top) and reference diffraction peaks for Mo and MoO_2 (bottom).

As the desired product had not formed, this synthesis was repeated, and the results are outlined below.

Characterization of P2

The second attempt of method 1 was first analyzed with SEM-EDS to determine particle sizes and elemental distribution (Figure 4.4). As shown in Figure 4.4a, the particle size distribution was uneven, and the particles were not confined to nanometer scale. Elemental mapping, revealed the presence of molybdenum, silicon, oxygen, and carbon. While carbon is typically attributed to the carbon tape used during sample preparation, a comparison of Figure 4.4b and 4.4e shows an overlap of both elements, indicating that carbon was also present in the material. Figure 4.4c and 4.4d highlight regions with increased amounts of silicon and oxygen, hinting to the formation of SiO_2.

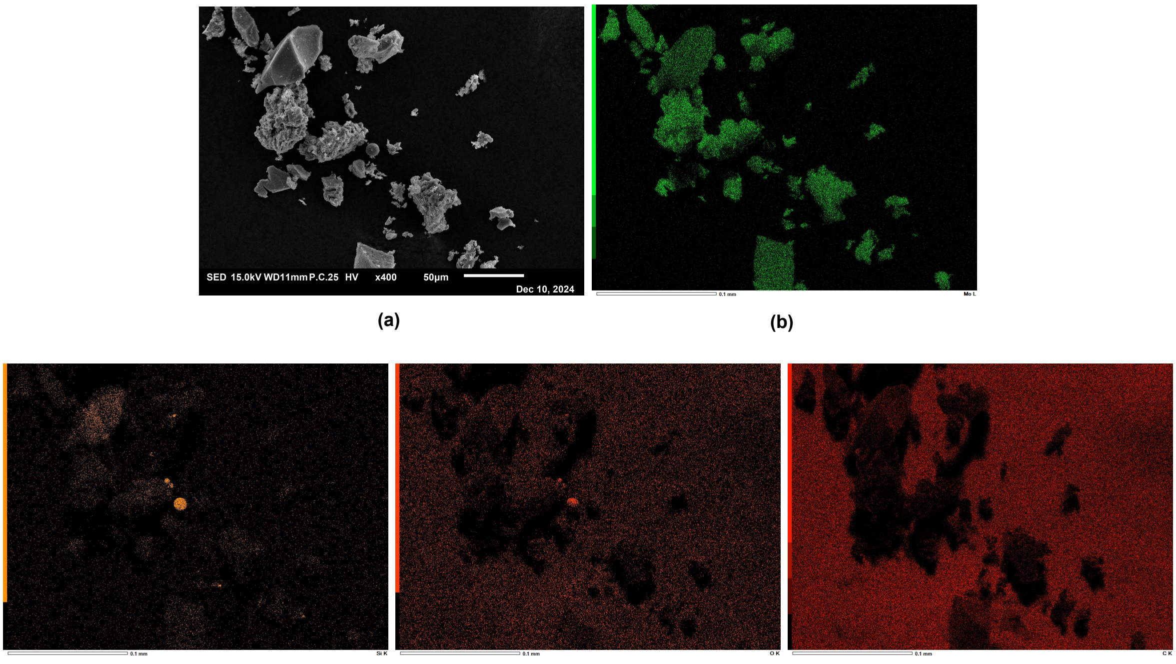

(a) **(b)**

(c) **(d)** **(e)**

Figure 4.4: Characterization of P2: **(a)** SEM image of EDS elemental mapped section, **(b)** Mo mapping, **(c)** Si mapping, **(d)** O Mapping and **(e)** C Mapping.

The phases in P2 were identified through XRD analysis (Figure 4.5). Similar to P1, no diffraction peaks corresponding to molybdenum silicides were observed. Instead, the product was found to be a mixture of molybdenum dioxide (PDF: 96-154-8821) and dimolybdenum carbide (PDF: 96-153-9796). The broadening of the peaks and the mismatch in relative intensities with references patterns, indicate a low crystallinity of the material.

The formation of MoO_2 can be attributed to the same reasoning as previously described for P1. As noted by J. Xu, et al. [87], sol-gel processes are ”established processes for the preparation of nanocrystalline oxides and carbides”. They further explain that carbides are likely formed firstly when using carbon as reduction agent, explaining the formation of Mo_2C.

Additionally, improper heat distribution caused by the malfunctioning tube furnace may have led to side reactions, preventing the formation of molybdenum silicides. Cracks in the tube may have allowed oxygen to leak into the system, further disrupting the reaction and contributing to the observed results.

Earlier EDS analysis showed possible formation of SiO_2. However, the absence of SiO_2 diffraction peaks in the XRD pattern, indicate it is probably amorphous.

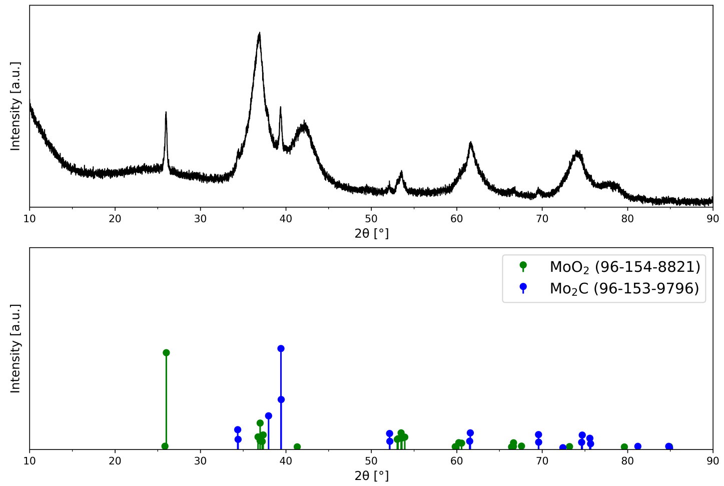

Figure 4.5: XRD pattern of P2 (top) and reference diffraction peaks for MoO_2 and Mo_2C (bottom).

Since this synthesis was performed twice, with both attempts failing to produce molybdenum silicides, the method was not further investigated, and alternate synthesis methods were explored.

4.1.2. Sol-gel and preoxidation method

Characterization of commercial $MoSi_2$

Figure 4.6a shows the SEM images taken of the commercial $MoSi_2$ material. The as-received $MoSi_2$ particles exhibit varying particle size and irregular shape, together with partially flat surfaces, as well as sharp or blunt edges. EDS mapping (Figure 4.6b, 4.6c) for Mo and Si showed a homogeneous distribution of elements. In addition, quantifying the elemental distribution of the sample resulted in the composition being 61.7 wt% Mo and 38.3 wt% Si, which show good agreement with the theoretical values for $MoSi_2$ of 63.1 and 36.9 wt%, respectively. The slight difference can be attributed to the relative error of ± 5% inherent in the quantification analysis performed using SEM-EDS [92].

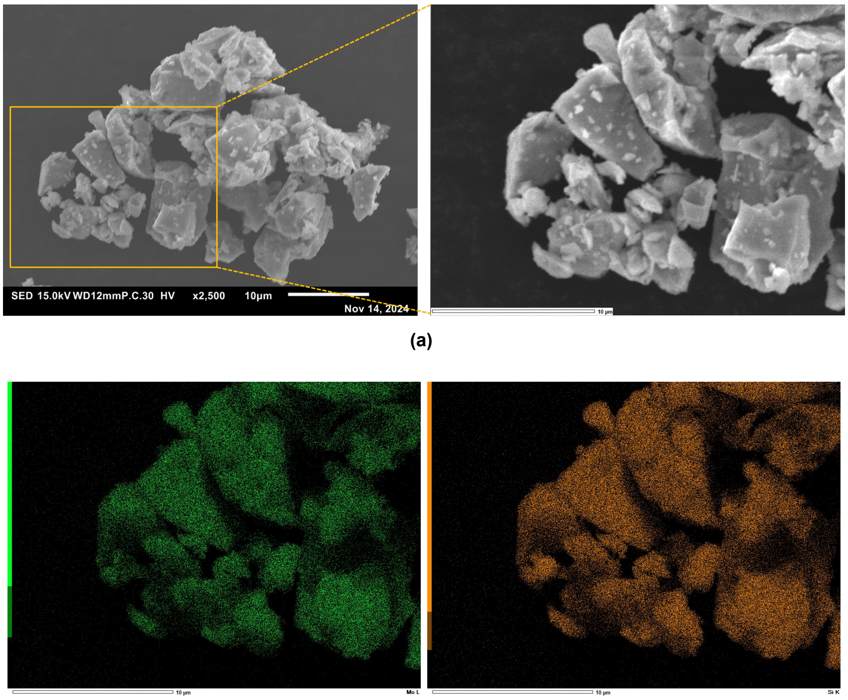

(a)

(b) (c)

Figure 4.6: Characterization of commercial $MoSi_2$: **(a)** SEM image with EDS elemental mapped section highlighted, **(b)** Mo mapping, **(c)** Si mapping.

The crystallinity and phase identification were analyzed using X-Ray Diffraction (XRD). Figure 4.7 (top) displays the obtained XRD pattern alongside the reference pattern for α-$MoSi_2$ (PDF: 96-101-0283) (bottom). The XRD pattern indicates high material crystallinity and purity, as no additional peaks are observed.

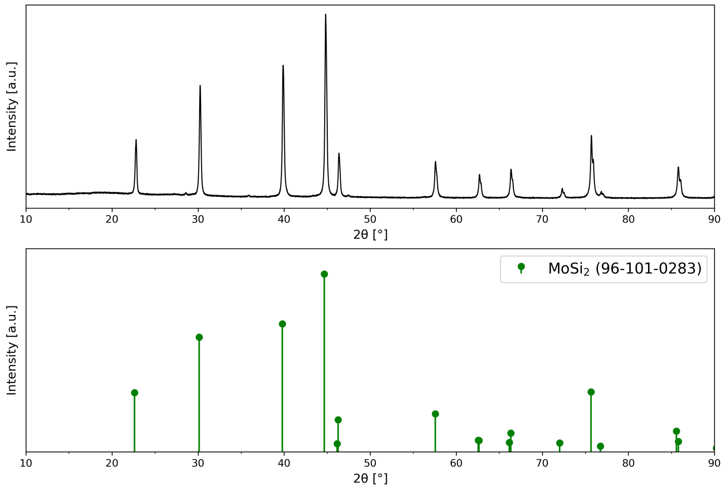

Figure 4.7: XRD pattern of commercial $MoSi_2$ material (top) and reference diffraction peaks for α-$MoSi_2$ (bottom).

Characterization of silica-coated $MoSi_2$

To improve the stability of $MoSi_2$ a silica coating can be formed around the material. This increases its low-temperature oxidation resistance by improving the structural integrity of the material [73]. The silica-coated $MoSi_2$ particles were prepared from commercial $MoSi_2$ material using a sol-gel process, followed by preoxidation at 800 °C (method 2). Figure 4.8a depicts SEM images taken of the final product. After coating the as-received $MoSi_2$, the size of the particles did not change and the material still exhibited varying particles size and irregular shape in the range of micrometers. Elemental mapping through EDS (Figure 4.8b, 4.8c and 4.8d) for Mo, Si and O showed a homogeneous distribution of elements. As EDS provides information on elements to a depth of 2 microns [83], it is expected that the X-Rays generated by the Mo atoms below the silica-coating can be measured as well.

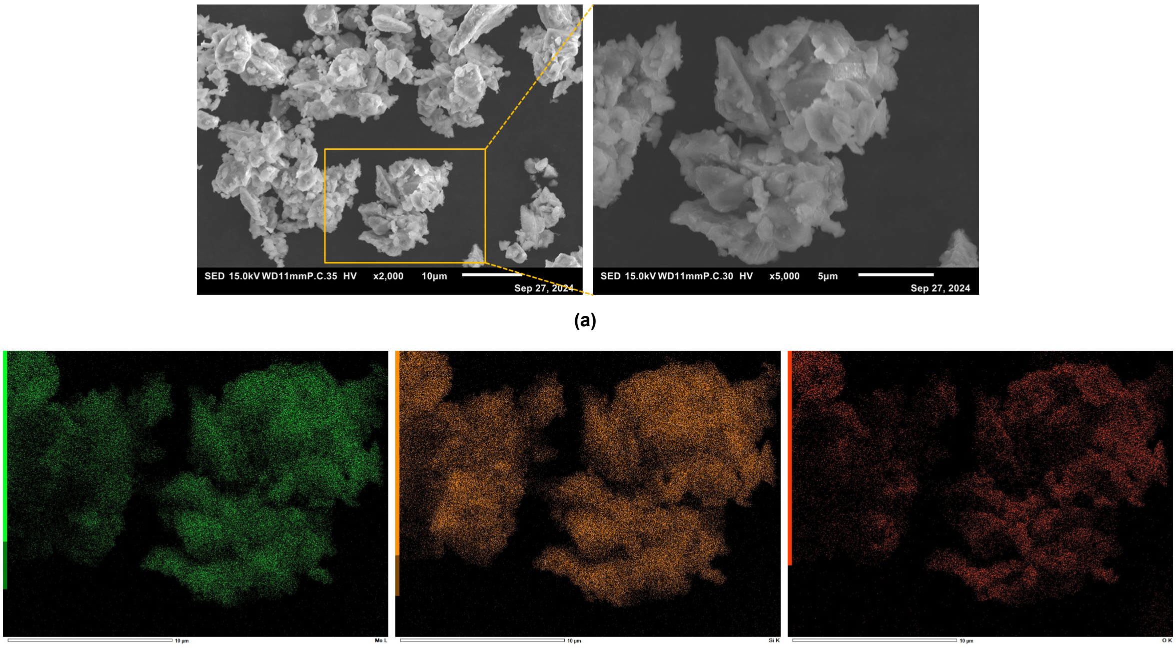

(a)

(b) (c) (d)

Figure 4.8: Characterization of silica-coated $MoSi_2$: **(a)** SEM image with EDS elemental mapped section highlighted, **(b)** Mo mapping, **(c)** Si mapping, **(d)** O mapping.

The surface chemical groups of the coated $MoSi_2$ material were analyzed using FTIR spectroscopy, with the spectra before and after coating presented in Figure 4.9. The FTIR spectrum of the uncoated material shows no significant absorption bands across the measured range. In contrast, the coated $MoSi_2$ exhibits absorption bands at approximately 1075 cm^{-1} and 800 cm^{-1}, corresponding to the asymmetric and symmetric stretching vibrations of the Si-O-Si network [93]. These findings confirm the presence of a silica encapsulating layer on the surface of the $MoSi_2$ particles.

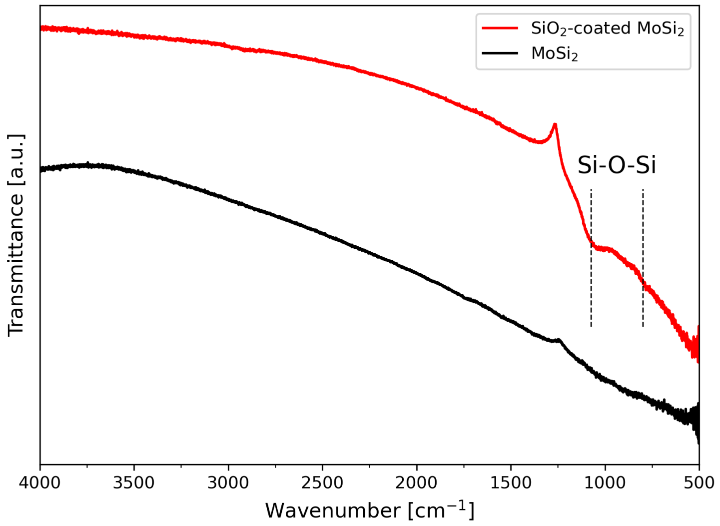

Figure 4.9: IR spectra of commercial $MoSi_2$ and the silica-coated $MoSi_2$.

The XRD spectrum of SiO_2-coated $MoSi_2$ (Figure 4.10, top) predominantly exhibits diffraction peaks corresponding to α-$MoSi_2$ (PDF: 96-101-0283), with additional low-intensity peaks attributed to Mo_5Si_3 (PDF: 96-153-7675). During preoxidation at 800 °C, two thermodynamically feasible oxidation reactions for $MoSi_2$ can occur [94]:

$$2\,\mathrm{MoSi_2(s)} + 7\,\mathrm{O_2(g)} \longrightarrow 4\,\mathrm{SiO_2(s)} + 2\,\mathrm{MoO_3\,(g)} \tag{4.3}$$

$$5\,\mathrm{MoSi_2(s)} + 7\,\mathrm{O_2(g)} \longrightarrow 7\,\mathrm{SiO_2(s)} + 2\,\mathrm{Mo_5Si_3(s)} \tag{4.4}$$

Both reactions have negative Gibbs free energy values, indicating spontaneity. As MoO_3 is volatile at 800 °C [95], it evaporates during heat treatment, leaving no trace in the final product. The presence of minor Mo_5Si_3 peaks in the XRD spectrum suggests partial oxidation of $MoSi_2$ via eq. 4.4.

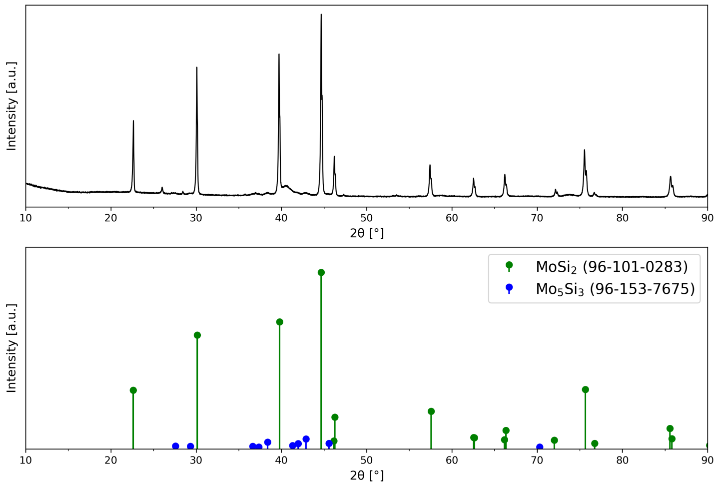

Figure 4.10: XRD pattern of SiO_2-coated $MoSi_2$ material (top) and reference diffraction peaks for α-$MoSi_2$ and Mo_5Si_3 (bottom).

The BET specific surface area of the SiO_2-coated $MoSi_2$ material was determined to be 11.19 ± 0.03 m^2/g. This value is consistent with the findings of Molotovska, Liliia, et al. [96], who reported specific surface areas of $MoSi_2$ particles in the range of 6 - 15 m^2/g for particle sizes between 0.1 and 5 µm. Although this reference is not directly related to the synthesis in this study, it supports the reasonableness of the observed surface area value.

4.1.3. Magnesiothermic reduction method

Characterization of intermediates

The first step in the synthesis of $Si/MoSi_2$ nanocomposites (method 3) was the preparation of SiO_2 nanoparticles. Figure 4.11a shows a SEM image of the resulting product, which reveals nanosphere structures with diameter between 300 - 400 nm. The XRD pattern of the SiO_2 precursor (Figure 4.11b, top) reveals its amorphous structure. Additionally, the SiO_2/MoO_3 intermediate product was analyzed via XRD, as shown in the same graph. A comparison with the reference pattern of MoO_3 (Figure 4.11b, bottom, PDF: 96-900-9670) indicates successful oxidation and incorporation of molybdenum. As the paper reported low Mo incorporation, the synthesis was adjusted to increase the Mo content. The XRD pattern of the SiO_2/MoO_3 intermediate with the increased Mo content is also shown in Figure 4.11b.

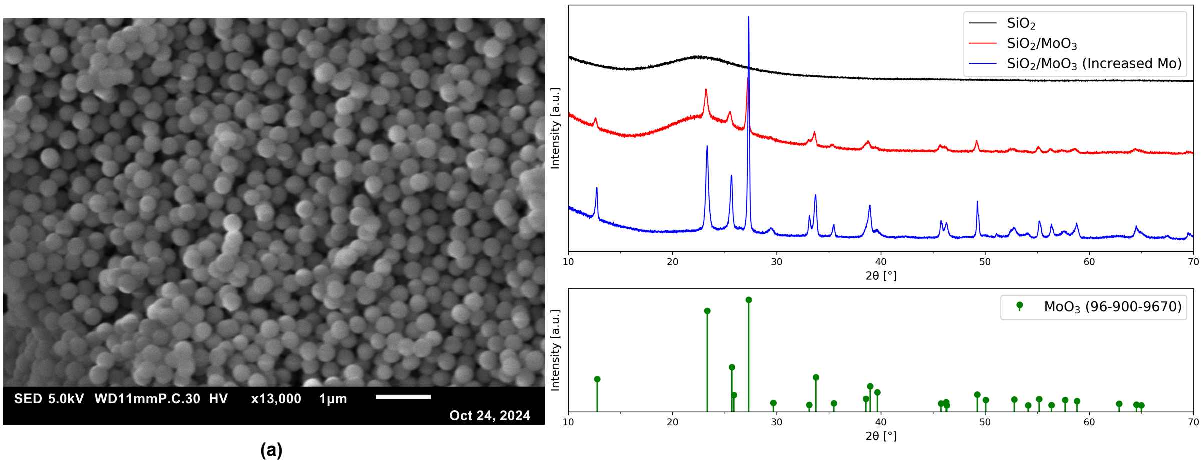

(a)

(b)

Figure 4.11: **(a)** SEM image of the synthesized SiO_2 precursor. **(b)** XRD pattern of the synthesized SiO_2 precursor (top), SiO_2/MoO_3 intermediate (middle) and SiO_2/MoO_3 intermediate with increased Mo content (bottom) along with the reference diffraction peaks for MoO_3.

Surface mapping with EDS was performed to acquire compositional data for both SiO_2/MoO_3 intermediates, as shown in Table 4.2. This clearly reveals an increase in the wt% of Mo.

Table 4.2: Weight percentage of Mo, Si and O elements in SiO_2/MoO_3 intermediates as determined by EDS elemental analyses.

	Mo	**Si**	**O**
SiO_2/MoO_3	0.57	28.73	70.70
SiO_2/MoO_3 (increased Mo)	23.96	10.69	65.35

Characterization of final products

Due to time limitations, only the original SiO_2/MoO_3 powder was used to try to synthesize the final products. The results of this are discussed below. XRD analysis was performed to determine whether the $Si/MoSi_2$ nanocomposites had been successfully synthesized (Figure 4.12). Analysis using Match! software identified several compounds in the sample, including MoO_2 (PDF: 96-154-88210), Si (PDF: 96-901-3109), $MgSiO_3$ (96-900-5903) and SiO_2 (PDF: 96-412-4054). However, no molybdenum silicides were detected.

According to the synthesis paper, the overall reactions occurring should be as follows:

$$\mathrm{SiO_2 + 2\,Mg \longrightarrow Si + 2\,MgO} \tag{4.5}$$
$$\mathrm{MoO_3 + 3\,Mg \longrightarrow Mo + 3\,MgO} \tag{4.6}$$
$$\mathrm{2\,Si + Mo \longrightarrow MoSi_2} \tag{4.7}$$

The heat released from the exothermic reactions (eq. 4.5 and 4.6) is intended to drive the formation of $MoSi_2$ (eq. 4.7).

The unsuccessful synthesis could be attributed to the extended heating time of the sample. Although the correct program was set for the tube furnace, it failed to cool down after the program had ended. Consequently, the sample remained at 700 °C for approximately 18 hours, instead of the desired 6 hours. A paper by Yan, M. et al. [97] reported that extended reaction times or improper magnesium quantities could lead to side reactions. One such side reaction, as shown in eq. 4.8, involves the formation of $MgSiO_3$ due to excessive heat buildup:

$$\mathrm{SiO_2 + MgO \longrightarrow MgSiO_3} \tag{4.8}$$

The heat buildup could be caused by the low molybdenum content in the oxide powder before reduction (Table 4.2). With insufficient molybdenum, eq. 4.7 cannot proceed effectively, preventing the utilization of heat from the exothermic reactions and allowing heat to build up inside the tube.
Additionally, the presence of MoO_2 and SiO_2 indicates incomplete magnesiothermic reduction, likely due to an insufficient amount of magnesium. Based on these observations, it was concluded that the synthesis should proceed using the oxide powder with higher molybdenum content. However, due to time limitations, this synthesis could not be performed.

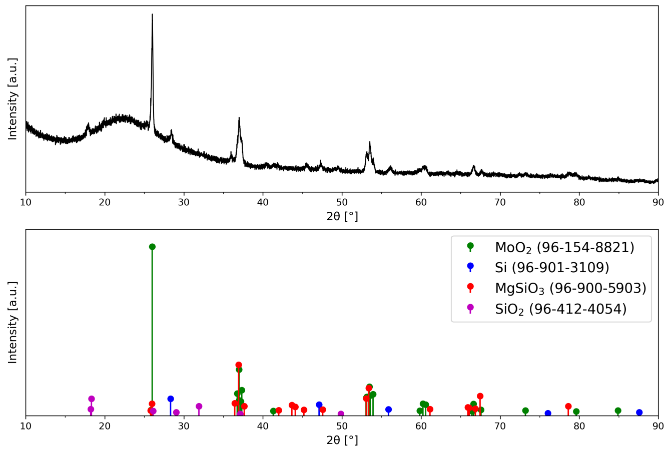

Figure 4.12: XRD pattern of the final product (top) and reference diffraction peaks for MoO_2, Si, $MgSiO_3$ and SiO_2 (bottom).

4.2. Chemical stability

The stability of the commercial and silica-coated $MoSi_2$ was evaluated in two different solutions, MilliQ and MEK. MilliQ was investigated due to its ability to provide a baseline for understanding the behavior of $^{99m}\mathrm{Tc}$ and $^{99}\mathrm{Mo}$ in a highly pure, polar solvent. MEK was investigated because of its proven efficacy in the solvent extraction of $^{99m}\mathrm{Tc}$, providing high separation efficiency for the extraction of $^{99m}\mathrm{Tc}$ from low-specific activity (n,γ) $^{99}\mathrm{Mo}$ [17][98][99]. Before investigating the extraction potential and retention behavior, the stability of the materials in these solutions at room temperature and atmospheric pressure was tested.

The results from the ICP-MS measurements of the washes of the commercial and silica-coated $MoSi_2$ materials are depicted below in Figure 4.13a and 4.13b, respectively. From the ten washes that were done on the material, wash 1–5 and the 10th wash are displayed. Both graphs show a lower molybdenum breakthrough in MEK when comparing it to data acquired from washes in MilliQ. At room temperature, $MoSi_2$ forms a layer of SiO_2 and MoO_3 [100]. MoO_3 is able to dissolve better in polar, aqueous solutions like MilliQ than in less-polar organic solvents like MEK, resulting in higher values for molybdenum breakthrough in MilliQ when compared to MEK [101]. This is again confirmed when looking at the stability of the materials after leaving them in solution, as can be seen in Figure 4.13c and 4.13d. Data on the first wash in MilliQ for commercial $MoSi_2$ has a large error. It is possible that the molybdenum was not evenly distributed in one of the samples when the 25 µL aliquot was taken for ICP-MS measurements, leading to a higher or lower concentration in the analyzed portion and causing variation between the triplicates. It is possible that the vials containing the first wash were not adequately homogenized during the preparation of the ICP-MS samples, leading to variations in the Mo content and resulting in a large error. Therefore, this experiment should be repeated to confirm the trend of a higher molybdenum breakthrough in MilliQ.

A comparison of the two materials reveals that coating with SiO_2 reduces molybdenum breakthrough. While the silica coating does not entirely prevent molybdenum leaching, it significantly limits the extent of leaching, thereby enhancing the material's stability. In MEK, both materials exhibit a relatively constant molybdenum loss after the first two washes, averaging $(2.5 \pm 0.7)\cdot 10^{-3}$ and $(0.9 \pm 0.2)\cdot 10^{-3}$% per wash for the commercial and coated $MoSi_2$, respectively. A similar trend is observed in MilliQ, but only for the coated material, where an average of $(0.4 \pm 0.1)\cdot 10^{-2}$% is washed off after the first two washes. From this, it can be concluded that most of the loosely bound or surface-accessible molybdenum is removed after the first two washes. For the non-coated material, this means that two washes are not enough to wash off the easily leachable molybdenum, and more washes are needed to reach a constant value.

Soaking the materials in MilliQ for 0, 1 and 24 hrs sequentially showed an increase in molybdenum breakthrough over time. For commercial $MoSi_2$ in MEK, the molybdenum breakthrough remained stable and did not increase. Molybdenum compounds exhibit higher solubility in MilliQ, leading to an increased leaching over time. In contrast, their solubility is limited in organic solvents like MEK [101]. This reduced solubility minimizes the leaching of molybdenum into the solvent, leading to stable breakthrough levels over time. For SiO_2-coated $MoSi_2$, the breakthrough after 24 hrs of soaking was lower than after 1 hr. This could be explained by the removal of a significant portion of easily leachable or surface-accessible molybdenum after 1 hr of soaking. With longer soaking times, the remaining molybdenum that could potentially leach out may have been minimal, leading to a reduction in breakthrough over time. To verify these conclusions, it is necessary to repeat these stability tests.

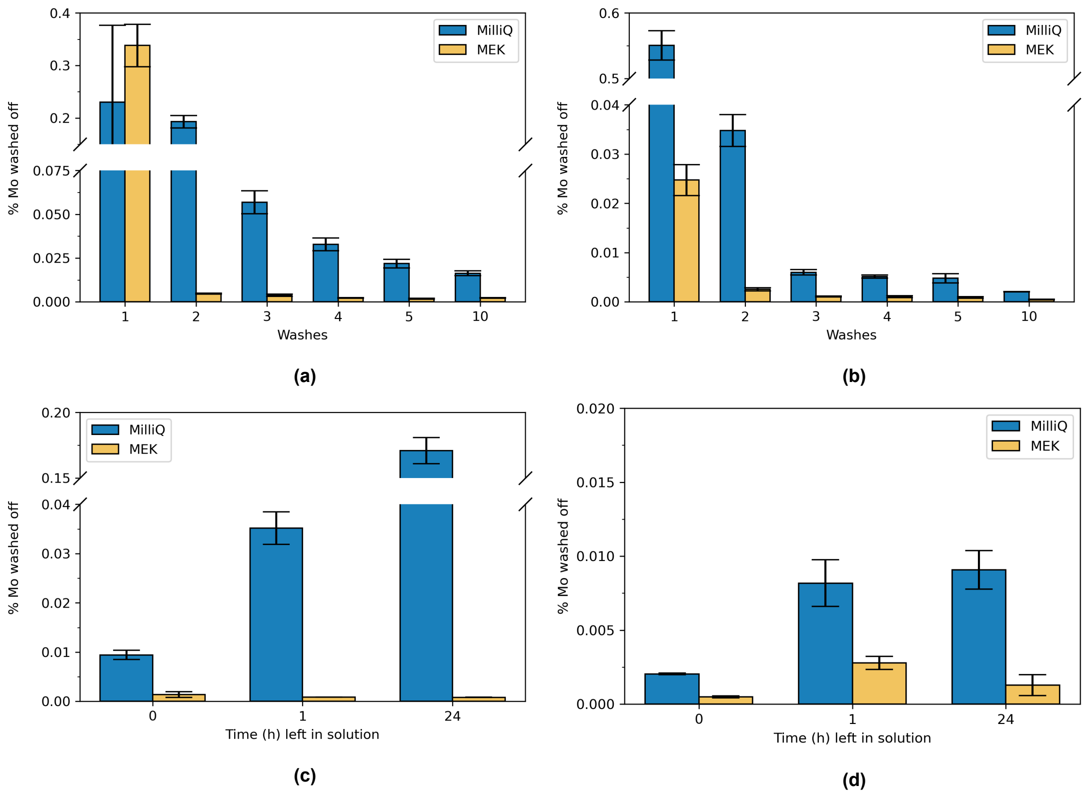

(a) (b) (c) (d)

Figure 4.13: Stability of $MoSi_2$ in chemical environments. The graphs show the percentage of Mo washed off over the course of 10 sequential washes in MilliQ and MEK for **(a)** commercial $MoSi_2$ and **(b)** silica-coated $MoSi_2$. Percentage of Mo washed off after soaking for 0, 1, or 24 hrs in **(c)** MilliQ and **(d)** MEK for commercial and silica-coated $MoSi_2$

A rough comparison with the regulatory amount of stable elements allowed in lutetium-177 solutions for radiolabeling can provide insights into the permissible amount of $^{98}\mathrm{Mo}$ that might leach into solution after 24 hours. Data on lutetium-177 is chosen due to the absence of data on allowable stable impurities in $^{99m}\mathrm{Tc}$, whereas limits for lutetium-177 are well-documented and are relevant for injectable radiopharmaceuticals [102]. This comparison helps determine whether the observed leaching levels are low enough for practical use, or if adjustments are necessary. The allowable contamination is typically in the range of µg/GBq or tens of µg/Ci. To produce 1 Ci of $^{99m}\mathrm{Tc}$, approximately 40 mg of $MoSi_2$ is required (Appendix A). Using this quantity, the estimated amount of $^{98}\mathrm{Mo}$ leached from commercial $MoSi_2$ is 68 ± 4 µg in MilliQ and 0.32 ± 0.02 µg in MEK. For silica-coated $MoSi_2$ the leaching value is significantly lower in MilliQ at 3.6 ± 0.5 µg, and similar in MEK at 0.5 ± 0.3 µg. These results indicate that MEK inherently limits breakthrough to very low levels, already falling below the regulatory threshold. Coating the material further reduces leaching, placing it well below the permissible limit. While this comparison is approximate and based on a rough estimation, it provides valuable insights into the behavior of the materials in different solvents.

4.3. Influence of media on ^{99}Mo and ^{99m}Tc extraction yield

Commercial and silica-coated $MoSi_2$ materials were irradiated and investigated for their extraction potential (Figure 4.14). Ideally, for the material to be effectively used in a new generation $^{99}\mathrm{Mo}/^{99m}\mathrm{Tc}$ generator, the highest amount of $^{99m}\mathrm{Tc}$ and lowest amount of $^{99}\mathrm{Mo}$ should be extracted. The oxidation states of $^{99}\mathrm{Mo}$ and $^{99m}\mathrm{Tc}$ during their extraction from $MoSi_2$ into MilliQ and MEK are influenced by the chemical environment of the solvent and the chemical behavior of $MoSi_2$ itself. When $MoSi_2$ is exposed to air or a medium like MilliQ containing dissolved oxygen, molybdenum tends to oxidize to its hexavalent state, forming MoO_3, which dissolves as the molybdate ion ($MoO_4{}^{2-}$) [103]. This aligns with a study by Shaw, L. [100] which shows that $MoSi_2$, when oxidized, forms a double oxide layer of SiO_2 and MoO_3, highlighting its tendency to stabilize as Mo(VI). Similarly, $^{99m}\mathrm{Tc}$ is likely to oxidize to its heptavalent state, forming $TcO_4{}^{-}$ [104]. In contrast, when $MoSi_2$ is dispersed in MEK, a non-oxidizing organic solvent, the oxidation environment is significantly milder. However, in an open system where atmospheric oxygen can dissolve into MEK, both nuclides will still be found as $MoO_4{}^{2-}$ and $TcO_4{}^{-}$ ions [105].

The results of the first extraction (Figure 4.14a) show a clear dependence on the solvent used. In MilliQ, both materials exhibit relatively higher extraction yields for both radionuclides compared to MEK. For commercial $MoSi_2$, the extraction yields for $^{99}\mathrm{Mo}$ and $^{99m}\mathrm{Tc}$ are nearly equal, at 2.2 ± 0.1% and 2.1 ± 0.2%. On the other hand, for the silica-coated material, $^{99m}\mathrm{Tc}$ is extracted more efficiently than $^{99}\mathrm{Mo}$, with a yield for $^{99m}\mathrm{Tc}$ of 1.7 ± 0.1%, while the $^{99}\mathrm{Mo}$ extraction yield is 0.5 ± 0.1%. This difference suggests that the silica coating influences interactions with the radionuclides. It is possible that the silica coating acts as a diffusion barrier, decreasing the oxidation and dissolution of molybdenum, thus limiting the formation of extractable $MoO_4{}^{2-}$ [73]. In contrast $^{99m}\mathrm{Tc}$, primarily present as the pertechnetate ion ($TcO_4{}^{-}$), is less impacted by the silica coating due to its reduced chemical interaction with the silica surface [106]. While the results for the first $^{99}\mathrm{Mo}$ and $^{99m}\mathrm{Tc}$ extraction from the silica-coated material in MilliQ look promising, the subsequent extractions do not substantiate this. To draw definitive conclusions, it would be necessary to repeat these experiments to confirm for reproducibility.

Furthermore, it is important to note that the first extraction also includes the contribution of recoiled atoms. During neutron irradiation, $^{98}\mathrm{Mo}$ undergoing the (n,γ) reaction can obtain sufficient kinetic energy to break its own chemical bonds and those of nearby molecules [107]. This phenomenon is therefore able to release $^{99}\mathrm{Mo}$ into the solvent. Because of this, the extraction yield of $^{99}\mathrm{Mo}$ in MilliQ is higher in the first extraction compared to the following extractions. In MEK this phenomenon is less pronounced due to the lower affinity of MEK for $MoO_4{}^{2-}$ [108].

The second extraction (Figure 4.14b) reveals a lower extraction yield in MilliQ compared to the first extraction. This reduction can be attributed to the absence of the contribution from the recoiling effect, as well as adsorption effects resulting from prolonged interaction with the solvent. The impact of this prolonged interaction will further be discussed in section 4.4. Notably, the lowered extraction yield is much more pronounced in MilliQ, while the second extraction yield in MEK is similar to the first. Additionally, the second extraction shows a greater difference between $^{99}\mathrm{Mo}$ and $^{99m}\mathrm{Tc}$ extraction yields in MEK compared to MilliQ, with a relatively higher extraction of $^{99m}\mathrm{Tc}$ and a lower extraction of $^{99}\mathrm{Mo}$. This can be explained by the increased affinity of pertechnetate ions ($^{99m}\mathrm{Tc}O_4{}^{-}$) for MEK [108]. In contrast, MilliQ, being a protic polar solvent [109], better facilitates the solubility of anions than aprotic solvents like MEK [110], resulting in more similar extraction yields for both radionuclides. The trends observed in the first two extractions are supported by the third extraction (Figure 4.14c).

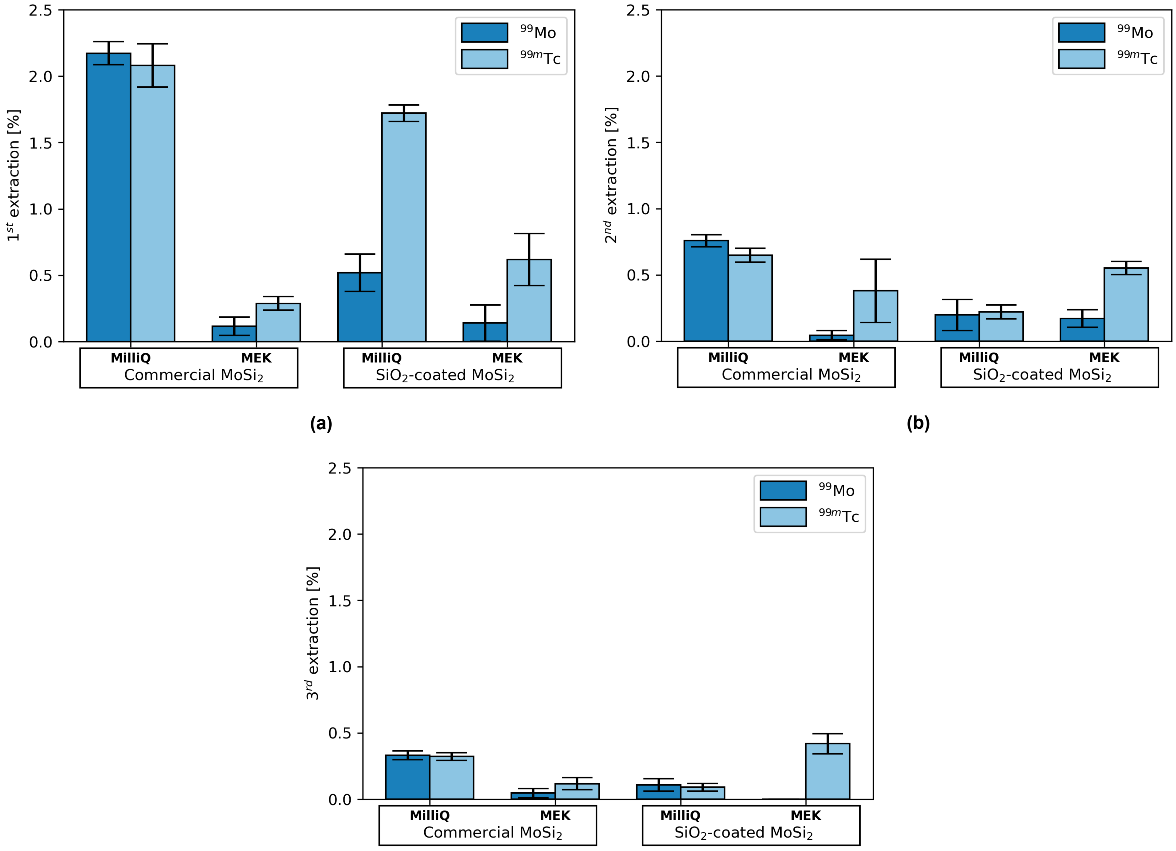

(a)

(b)

(c)

Figure 4.14: Influence of media on extraction yield of ^{99}Mo and ^{99m}Tc: Extraction after **(a)** 0, **(b)** 24 and **(c)** 48 hrs.

Comparing the two materials and solvents, the most promising results are achieved with the silica-coated material in MEK, which shows the largest relative difference between ^{99}Mo and ^{99m}Tc extraction yields favoring ^{99m}Tc extraction. Despite these promising trends, the overall extraction yields remain relatively low. To improve these yields, increasing the surface area of the materials is necessary to facilitate more interaction with the solvent. This can possibly be achieved by using nanoparticles, as is substantiated by a study into molybdenum sulfide materials, which showed increased extraction yields with nanosized materials [111]. Specifically, the extraction efficiency of ^{99m}Tc from molybdenum sulfide materials with specific surface areas of 124.6 ± 35.39 m^2/g and 15 ± 9.53 m^2/g was 12.6 ± 0.50% and 3.0 ± 0.79%, respectively, in MEK. These findings highlight that an increased surface area may enhance the extraction efficiency.

4.4. Influence of media on ^{99}Mo and ^{99m}Tc retention in the material

Lastly, the influence of the media on the retention of ^{99}Mo and ^{99m}Tc in the commercial and silica-coated materials was investigated. Retention refers to the proportion of a radionuclide that remains attached to the material after interaction with the solvent, as opposed to extraction, which measures the fraction of radionuclide released into the solvent. These experiments were done to gain insights in the selectivity of radionuclide interactions with the materials. Ideally, ^{99}Mo retention should be high to minimize its extraction alongside ^{99m}Tc. On the other hand, low retention of ^{99m}Tc is favorable to maximize its extraction yield.

Retention of the radionuclides was initially measured over a short time period by passing the stock solution through the materials without soaking (Figure 4.15a). In MilliQ, the silica-coated material showed less retention of both radionuclides, indicating that the SiO_2-coating may inhibit the adsorption of $^{99}\mathrm{Mo}$ and $^{99m}\mathrm{Tc}$. At neutral pH, SiO_2 surfaces can acquire a negative charge due to deprotonation of silanol groups [112]. This negative surface charge can repel anionic species like $MoO_4{}^{2-}$ and $TcO_4{}^{-}$, resulting in a decreased adsorption. For experiments in MEK, retention data for $^{99}\mathrm{Mo}$ is absent due to the low initial extraction of $^{99}\mathrm{Mo}$ in the MEK stock solution, which resulted in insufficient gamma counts and high uncertainties. $^{99m}\mathrm{Tc}$ retention in the silica-coated material was lower than in the commercial material. MEK can engage in hydrogen bonding with silanol groups present on the silica surface [113]. This occupation of silanol groups by MEK reduces the number of active sites accessible for radionuclide adsorption.

In the second set of retention measurements, the materials were soaked in the stock solution for 24 hours (Figure 4.15b). In general, retention values increased for all samples, indicating that prolonged contact time facilitates adsorption [114]. After 24 hours in MilliQ, similar results were obtained for both materials and radionuclides, indicating that the SiO_2-coating had no significant effect on adsorption under these conditions. As in the short-term experiments, no retention data for $^{99}\mathrm{Mo}$ in MEK is presented due to insufficient gamma counts caused by the low initial extraction of $^{99}\mathrm{Mo}$ into the MEK stock solution. For $^{99m}\mathrm{Tc}$, retention in the silica-coated material remained consistently lower than in the commercial material after 24 hours of soaking. This reduced retention is likely due to the interaction of MEK with silanol groups on the silica surface, as mentioned before.

The observed difference in retention between the two materials in two different solvents, highlights the critical role of solvent interactions in governing radionuclide adsorption. This emphasizes that the retention behavior is not only dependent on the material's properties, but also on the medium in which the experiments are done. Combined with the low extraction of $^{99}\mathrm{Mo}$ in MEK as previously discussed in section 4.3, the lowest retention of $^{99m}\mathrm{Tc}$ after 24 hours makes the silica-coated material in MEK the most promising of the investigated options.

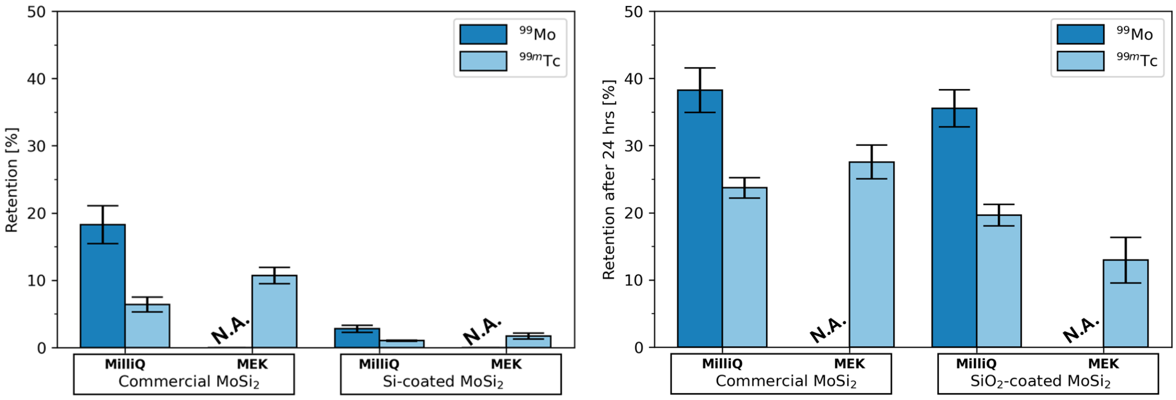

(a) (b)

Figure 4.15: Influence of media on the retention of $^{99}\mathrm{Mo}$ and $^{99m}\mathrm{Tc}$ after **(a)** 0 and **(b)** 24 hrs.

5

Conclusions

This study investigated the production and viability of molybdenum silicide (nano)materials as irradiation targets for a new generation $^{99}\mathrm{Mo}$/$^{99m}\mathrm{Tc}$ generator. In this generator, the material will be used as both the target material for neutron-activated $^{99}\mathrm{Mo}$ production and generator material for $^{99m}\mathrm{Tc}$ extraction. The production of molybdenum silicides was investigated through different synthesis methods: a combination of sol-gel and carbothermic reduction method, a sol-gel preoxidation method, and a magnesiothermic reduction method. Through characterization, stability tests and irradiation experiments, key insights into the performance and limitations of these materials were obtained.

The sol-gel and carbothermic reduction method failed to produce molybdenum silicides, yielding elemental molybdenum and molybdenum dioxide, as confirmed by XRD analysis. This incomplete reduction was likely caused by oxygen contamination in the tube furnace. A second attempt produced molybdenum dioxide and molybdenum carbide and also failed, prompting the use of alternative synthesis methods. The sol-gel preoxidation method successfully formed an amorphous silica coating around commercial molybdenum silicide, confirmed by Si-O-Si absorption bands in IR spectra and XRD analysis. SEM revealed micrometer-scale particle sizes. Synthesis of Si/$MoSi_2$ nanocomposites was partially successful. An intermediate with nanosphere structures (300 - 400 nm) was synthesized, containing MoO_3 and amorphous SiO_2. Initially, the intermediate had a low Mo content (0.57 wt%), which was later increased to 23.96 wt%. Attempts to use the low-Mo intermediate for nanocomposite synthesis resulted in MoO_2, Si, $MoSiO_3$ and SiO_2, as shown by XRD analysis. Further synthesis with the high-Mo intermediate was planned, but could not be completed due to time limitations.

Experiments on the chemical stability of commercially available and silica-coated $MoSi_2$ were done in MilliQ and MEK. Silica-coated $MoSi_2$ demonstrated a lower molybdenum breakthrough in both solvents. In MEK both materials showed a relatively constant molybdenum loss after 2 washes, averaging $(2.5 \pm 0.7)\cdot 10^{-3}$ and $(0.9 \pm 0.2)\cdot 10^{-3}\%$ per wash for the commercial and coated $MoSi_2$, respectively. A similar result was obtained in MilliQ for the silica-coated $MoSi_2$ with an average of $(0.4 \pm 0.1)\cdot 10^{-2}\%$ of molybdenum washed off after the first two washes, concluding that most of the loosely bound or surface accessible molybdenum is removed after the first two washes.

Extraction measurements from these materials showed an increased extraction of both radionuclides in MilliQ. However, the second and third extraction showed a more favorable extraction in MEK where relatively more $^{99m}\mathrm{Tc}$ was extracted and a lower amount of $^{99}\mathrm{Mo}$ was extracted. The most promising results were found for the silica-coated material in MEK which showed the largest relative difference between $^{99}\mathrm{Mo}$ and $^{99m}\mathrm{Tc}$ extraction yields, favoring $^{99m}\mathrm{Tc}$ extraction. However, the overall extraction yields remained relatively low.

The retention studies showed that solvent interactions significantly influence radionuclide adsorption in both commercial and silica-coated materials. In MilliQ, the silica-coated material exhibited lower initial retention for $^{99}\mathrm{Mo}$ and $^{99m}\mathrm{Tc}$, likely due to the silica's surface negative charge repelling anionic species. After 24 hours, retention values increased, indicating time-dependent adsorption processes. In MEK, retention for $^{99}\mathrm{Mo}$ could not be evaluated due to low initial extraction, but $^{99m}\mathrm{Tc}$ retention was lower in the silica-coated material, attributed to reduced active sites from solvent interactions with silanol groups. These findings highlight that the silica-coated material in MEK, with lower $^{99m}\mathrm{Tc}$ retention and limited $^{99}\mathrm{Mo}$ extraction, shows promising results for its use in new $^{99}\mathrm{Mo}$/$^{99m}\mathrm{Tc}$ generators.

6

Recommendations

Several suggestions for additional research are made in light of the findings and conclusions from this project.

The successful synthesis of a Si/$MoSi_2$ nanocomposite should be pursued with the aim of producing nanosized particles with a higher surface area. This is expected to significantly increase the extraction potential of radionuclides, as the increased surface area facilitates greater interaction between the solvent and the particle surface. Additionally, the molybdenum content in the material could be further increased, possibly by increasing the amount of ammonium heptamolybdate tetrahydrate used during this synthesis. This could result in higher radionuclide extraction yields per unit mass of material.

The use of nanoparticles, due to their higher surface area-to-volume ratio, could increase the extraction potential, but would possibly also facilitate greater adsorption [115]. While this increased retention may counteract the desired selectivity, the potential for nanoparticles to enhance radionuclide extraction remains an important factor to consider. To mitigate this, surface modifications of the silica coating could be employed to reduce the retention. For instance, hydrophobic groups introduced via methyl trimethoxy silane (MTMS) could decrease the adsorption of polar or ionic species like $TcO_4{}^-$. By carefully optimizing nanoparticle design and surface chemistry, it may be possible to maximize extraction efficiency while maintaining selectivity.

Furthermore, the silica coating has showed promising results in the enhancement of the material's stability while yielding relatively good extraction results in MEK. Building on this, in the future, Si/$MoSi_2$ nanocomposites with a silica coating could be synthesized and further investigated. This approach could combine the benefits of nanosized particles, having a larger surface area, with the enhanced stability of the silica coating. Would these syntheses be successful, the material's stability as well as their extraction and retention potentials could be investigated. This would hopefully lead to higher extraction yields together with high material stability in solvents.

The stability tests conducted on commercial $MoSi_2$ in MilliQ showed some variability, particularly in the first wash. To address this, the experiment should be repeated to obtain more accurate and consistent data. Additionally, stability tests over time should be repeated for the SiO_2-coated material in MEK to verify and refine the conclusions drawn from the initial experiments. This will help ensure that the data is reliable and reproducible.

In order for the extracted $^{99m}\mathrm{Tc}$ to be used for medical applications, the $^{99m}\mathrm{Tc}$ has to be extracted from MEK with a purity that complies with EU Pharmacopeia regulations — this value being 0.1 μCi of $^{99}\mathrm{Mo}$ / mCi $^{99m}\mathrm{Tc}$ in the eluted product at the time of administration [116]. Would it be needed to extract the impurities, the solutions could be purified by a combination of a small alumina column to remove traces of Mo and a MEK evaporator to remove MEK from the final product. This has already been investigated by Chattopadhyay, S., et al. [104].

Bibliography

[1] World Health Organization. *Cancer*. Accessed: 2024-11-21. 2022. URL: `https://www.who.int/news-room/fact-sheets/detail/cancer`.

[2] Sajid Mushtaq, Asia Bibi, Jung Eun Park, and Jongho Jeon. “Recent progress in technetium-99m-labeled nanoparticles for molecular imaging and cancer therapy”. In: *Nanomaterials* 11.11 (2021), p. 3022.

[3] Karl Heinrich Lieser. *Nuclear and radiochemistry: fundamentals and applications*. John Wiley & Sons, 2008.

[4] Mohamed F. Nawar and A. Türler. “New strategies for a sustainable 99mTc supply to meet increasing medical demands: Promising solutions for current problems”. In: *Frontiers in Chemistry* 10 (July 2022), p. 926258. ISSN: 22962646. DOI: `10.3389/fchem.2022.926258`.

[5] Jonathan R Dilworth and Sofia I Pascu. “The radiopharmaceutical chemistry of technetium and rhenium”. In: *The chemistry of molecular imaging* (2014), pp. 137–164.

[6] Ali Torkamani, Ali Taghibi Khotbehsara, Faezeh Rahmani, Alexander Khelvas, Alexander Bugaev, and Farshad Ghasemi. “Conceptual design of hybrid target for molybdenum-99 production based on heavywater”. In: *Nuclear Engineering and Technology* 55.5 (2023), pp. 1863–1870.

[7] International Atomic Energy Agency. “Non-HEU Production Technologies for Molybdenum-99 and Technetium-99m”. In: *IAEA Nuclear Energy Series No. NF-T-5.4* (2013).

[8] Maheshwar Sharon and Madhuri Sharon. *Nuclear chemistry*. Springer, 2021.

[9] Seung-Kon Lee, Gerd J Beyer, and Jun Sig Lee. “Development of industrial-scale fission 99Mo production process using low enriched uranium target”. In: *Nuclear Engineering and Technology* 48.3 (2016), pp. 613–623.

[10] AI Ryabchikov, VS Skuridin, EV Nesterov, EV Chibisov, and VM Golovkov. “Obtaining molybdenum-99 in the IRT-T research reactor using resonance neutrons”. In: *Nuclear Instruments and Methods in Physics Research Section B: Beam Interactions with Materials and Atoms* 213 (2004), pp. 364–368.

[11] Maria Lyra, Paraskevi Charalambatou, Eirini Roussou, Stavros Fytros, and Irini Baka. “Alternative production methods to face global molybdenum-99 supply shortage.” In: *Hellenic Journal of Nuclear Medicine* 14.1 (2011), pp. 49–55.

[12] Plexus scientific. *Specific Activities*. Accessed: 2025-01-09. 2025. URL: `http://www.iem-inc.com/information/tools/specific-activities`.

[13] Steven C Van der Marck, Arjan J Koning, and Kevin E Charlton. *The options for the future production of the medical isotope 99 Mo*. 2010.

[14] Cecilia C Guedes-Silva, Thiago dos Santos Ferreira, Flávio Carvalho, Carolina M de Paula, and Larissa Otubo. “Influence of alumina phases on the molybdenum adsorption capacity and chemical stability for 99 Mo/99m Tc generators columns”. In: *Materials Research* 19 (2016), pp. 791–794.

[15] Shameem Hasan and Mark A Prelas. “Molybdenum-99 production pathways and the sorbents for 99Mo/99mTc generator systems using (n, γ) 99Mo: a review”. In: *SN Applied Sciences* 2.11 (2020), p. 1782.

[16] Ashutosh Dash, F. F. Knapp, and M. R.A. Pillai. “99Mo/99mTc separation: An assessment of technology options”. In: *Nuclear Medicine and Biology* 40 (2 Feb. 2013), pp. 167–176. ISSN: 0969-8051. DOI: `10.1016/J.NUCMEDBIO.2012.10.005`.

[17] Sankha Chattopadhyay, Sujata Saha Das, Luna Barua, Asit Kumar Pal, Umesh Kumar, Md Nayer Alam, Arup Kumar Hudait, Sharmila Banerjee, et al. “A compact solvent extraction based

99Mo/99 mTc generator for hospital radiopharmacy". In: *Applied Radiation and Isotopes* 143 (2019), pp. 41–46.

[18] Rubel Chakravarty, SK Sarkar, Meera Venkatesh, and Ashutosh Dash. "An electrochemical procedure to concentrate 99mTc availed from a zirconium [99Mo] molybdate gel generator". In: *Applied Radiation and Isotopes* 70.2 (2012), pp. 375–379.

[19] Z. Yao, J. Stiglich, and T.S. Sudershan. "Molybdenum silicide based materials and their properties". In: *Journal of Materials Engineering and Performance* 8 (3 June 1999), pp. 291–304. ISSN: 10599495. DOI: `10.1361/105994999770346837/METRICS`. URL: `https://link.springer.com/article/10.1361/105994999770346837`.

[20] Jianguang Xu, Yu Zhang, Jinshun Qi, Yu Wang, Juhua Luo, and Wei Yao. "Preparation of nanocrystalline MoSi 2 with enhanced lithium storage by sol-gel and carbonthermal reduction method". In: (2018). Sol-gel method to synthesize MoSi2 nanoparticles. DOI: `10.1016/j.ceramint.2018.02.167`. URL: `https://doi.org/10.1016/j.ceramint.2018.02.167`.

[21] Sugam Kumar and VK Aswal. "Tuning of nanoparticle–surfactant interactions in aqueous system". In: *Journal of Physics: Condensed Matter* 23.3 (2010), p. 035101.

[22] Shameem Hasan and Mark A. Prelas. "Molybdenum-99 production pathways and the sorbents for 99Mo/99mTc generator systems using (n, γ) 99Mo: a review". In: *SN Applied Sciences* 2 (11 Nov. 2020), pp. 1–28. ISSN: 25233971. DOI: `10.1007/S42452-020-03524-1/TABLES/6`. URL: `https://link.springer.com/article/10.1007/s42452-020-03524-1`.

[23] N/A. *Medical Isotope Production Without Highly Enriched Uranium*. National Academies Press, May 2009. ISBN: 9780309130394. DOI: `10.17226/12569`. URL: `http://dx.doi.org/10.17226/12569`.

[24] D Milian, DE Milian, M Cadavid, LP Rodriguez, and J Salomón. "Feasibility neutronic conceptual design for the core configuration of a 75 kWth aqueous homogeneous reactor for 99Mo production". In: *Proceeding of XV Workshop on Nuclear Physics and IX Symposium on Nuclear & Related Techniques*. 2015.

[25] International Atomic Energy Agency. *Nuclear Data Section*. Accessed: 12-09-2024. 2024. URL: `https://www-nds.iaea.org/`.

[26] Victor J Molinski. "A review of 99mTc generator technology". In: *The International Journal of Applied Radiation and Isotopes* 33.10 (1982), pp. 811–819.

[27] DS Sairanbayev, Sh Kh Gizatulin, AN Gurin, Ye T Chakrova, MT Aitkulov, A Zh Nessipbay, A Ch Ashibayev, and AA Shaimerdenov. "Optimizing irradiation conditions for natural molybdenum in WWR-K reactor". In: *Nuclear Engineering and Technology* (2024).

[28] Vladimir Radulović, Nicolas Thiollay, Hubert Carcreff, Anže Pungerčič, Klemen Ambrožič, Christophe Destouches, and Andrej Trkov. "Epithermal neutron activation dosimetry–(n, γ) reactions under boron-based filters". In: *Scientific Reports* 14.1 (2024), p. 28604.

[29] Kirk Bertsche. "Accelerator production options for 99Mo". In: *Proceedings of IPAC* 10.08 (2010), p. 121.

[30] AA Alharbi, A Azzam, M McCleskey, B Roeder, A Spiridon, E Simmons, VZ Goldberg, A Banu, L Trache, and RE Tribble. "Medical radioisotopes production: a comprehensive cross-section study for the production of Mo and Tc radioisotopes via proton induced nuclear reactions on natMo". In: *Radioisotopes-Applications in Bio-Medical Science*. IntechOpen, 2011.

[31] Kamel Abbas, Uwe Holzwarth, Federica Simonelli, Jan Kozempel, Izabela Cydzik, Antonio Bulgheroni, Giulio Cotogno, Christos Apostolidis, Frank Bruchertseifer, and Alfred Morgenstern. "Feasibility of 99Mo production by proton-induced fission of 232Th". In: *Nuclear Instruments and Methods in Physics Research Section B: Beam Interactions with Materials and Atoms* 278 (2012), pp. 20–25.

[32] Yasuki Nagai and Yuichi Hatsukawa. "Production of 99Mo for nuclear medicine by 100Mo (n, 2 n) 99Mo". In: *Journal of the Physical Society of Japan* 78.3 (2009), p. 033201.

[33] Riya Gupta and Muhammad F. Hashmi. “Mo99 - Tc99m Generator”. In: *StatPearls* (July 2023). URL: `https://www.ncbi.nlm.nih.gov/books/NBK565854/`.

[34] A Mushtaq. “Inorganic ion-exchangers: their role in chromatographic radionuclide generators for the decade 1993–2002”. In: *Journal of Radioanalytical and Nuclear Chemistry* 262.3 (2004), pp. 797–810.

[35] International Atomic Energy Agency (IAEA). *Alternative ^{99}Mo-^{99m}Tc Generator Designs*. `https://humanhealth.iaea.org/HHW/Radiopharmacy/VirRad/Eluting_the_Generator/Generator_Module/Design_principles/Alternative_99Mo-99mTc_generator_designs/index.html`. Accessed: 2024-06-17. n.d.

[36] J A Osso, M F Catanoso, G Barrio, T P Brambilla, R Teodoro, C RBR Dias, and K N Suzuki. “Technetium-99m–New production and processing strategies to provide adequate levels for SPECT imaging”. In: *Current Radiopharmaceuticals* 5.3 (2012), pp. 178–186.

[37] Jens-Volker Kratz. *Nuclear and radiochemistry: Fundamentals and applications*. John Wiley & Sons, 2022.

[38] Ilse Zolle. “Performance and quality control of the 99Mo/99mTc generator”. In: *Technetium-99m Pharmaceuticals: Preparation and Quality Control in Nuclear Medicine*. Springer, 2007, pp. 77–93.

[39] Ronaldo Thibes and Suzicleide L de Oliveira. “General solution to Bateman’s differential equations with direct index notation”. In: *International Journal of Pure and Applied Mathematics* 93 (6 2014), pp. 879–883. ISSN: 1314-3395. DOI: `10.12732/ijpam.v93i6.11`.

[40] Adon A Gordus. “Hot-atom chemistry”. In: *Journal of radioanalytical and nuclear chemistry* 142 (1990), pp. 293–301.

[41] Casimiro S Munita, Michael D Glascock, and Roberto Hazenfratz. “Neutron activation analysis: an overview”. In: *Recent advances in analytical techniques* 3 (2019), pp. 179–227.

[42] Gregory Choppin, Jan-Olov Liljenzin, Jan Rydberg, and Christian Ekberg. *Radiochemistry and nuclear chemistry*. Academic Press, 2013.

[43] Bhupendra S Tomar, Olav M Steinebach, BE Terpstra, P Bode, and H Th Wolterbeek. “Studies on production of high specific activity 99Mo and 90Y by Szilard Chalmers reaction”. In: *Radiochimica Acta* 98.8 (2010), pp. 499–506.

[44] Xingchen Liu, Dongbo Cao, Tao Yang, Hao Li, Hui Ge, Manuel Ramos, Qing Peng, Albert K Dearden, Zhi Cao, Yong Yang, et al. “Insight into the structure and energy of Mo 27 S x O y clusters”. In: *RSC Advances* 7.16 (2017), pp. 9513–9520.

[45] JLTM Moret. “Novel approaches to produce radionuclides using hot atom chemistry principles”. In: (2020).

[46] Peter Crowther and JS Eldridge. “Decay of 99Mo-99mTc”. In: *Nuclear Physics* 66.2 (1965), pp. 472–480.

[47] Hubert Theodor Wolterbeek and Peter Bode. *Process for the production of no-carrier added 99 mo*. US Patent App. 12/996,209. 2011.

[48] A Schwartz, R Rafaeloff, and E Yellin. “The Szilard-Chalmers reaction on gallium phthalocyanine in high neutron flux”. In: *The International Journal of Applied Radiation and Isotopes* 20.12 (1969), pp. 853–857.

[49] LA Fucugauchi, S Millan, A Mondragon, and M Solache-Rios. “Chemical effects of (n, γ) nuclear reaction on (Mo 6 Cl 8) Cl 4”. In: *Journal of radioanalytical and nuclear chemistry* 178 (1994), pp. 437–442.

[50] MINH CHU NGO. “Development of β-MoO3 targets for 99Mo/99mTc isotope preparation utilizing hot atoms”. In: (2022).

[51] LI Menshikov, AN Semenov, and D Yu Chuvilin. “Calculation of the escape of the recoil atoms in the reaction 98Mo (n, γ) 99Mo from molybdenum (iv) disulfide nanoparticles”. In: *Atomic Energy* 114.4 (2013), pp. 280–284.

[52] JLTM Moret, TA Hardens, O van Batenburg, HT Wolterbeek, JR van Ommen, and AG Denkova. “64Cu enrichment using the Szilard-Chalmers effect–The influence of γ-dose”. In: *Applied Radiation and Isotopes* 160 (2020), p. 109135.

[53] Xiangrong Hu, Yoshitaka Fujita, Kunihiko Tsuchiya, Satoshi Fukutani, Jun-ichi Hori, and Tatsuya Suzuki. “Water extraction of technetium-99m from neutron irradiated porous molybdenum dioxide pellet”. In: *Journal of Radioanalytical and Nuclear Chemistry* (2024), pp. 1–7.

[54] NM Quach, MC Ngo, Y Yang, TB Nguyen, VT Nguyen, Y Fujita, TMD Do, T Nakayama, T Suzuki, and H Suematsu. “Extraction of 99Mo hot atoms made by a neutron capture method from α-MoO3 to water”. In: *Journal of Radioanalytical and Nuclear Chemistry* 332.10 (2023), pp. 4057–4064.

[55] JFW Nijsen, AD van Het Schip, MJ Van Steenbergen, SW Zielhuis, LMJ Kroon-Batenburg, M Van de Weert, PP Van Rijk, and WE Hennink. “Influence of neutron irradiation on holmium acetylacetonate loaded poly (L-lactic acid) microspheres”. In: *Biomaterials* 23.8 (2002), pp. 1831–1839.

[56] Yanyan Su, Yusheng Xie, Haoran Qin, Zixun Huang, Qiaofei Yin, Zhiwang Li, Rongbin Zhang, Zepeng Zhao, Fengchi Wu, and Gang Ou. “Ultrafine molybdenum silicide nanoparticles as efficient hydrogen evolution electrocatalyst in acidic medium”. In: *International Journal of Hydrogen Energy* 47 (67 Aug. 2022). Mo5Si3 and MoSi2 nanoparticle synthesis through molten salt reduction method, pp. 28924–28931. ISSN: 0360-3199. DOI: `10.1016/J.IJHYDENE.2022.06.218`.

[57] Foundry Technologies and Engineering GmbH. *Intermetallic Phase*. Accessed: 2024-12-18. n.d. URL: `https://www.giessereilexikon.com/en/foundry-lexikon/Encyclopedia/show/intermetallic-phase-4565/?cHash=fc50d9a4ec7a9ad5757902d9d229d24f`.

[58] R. Mitra. “Molybdenum silicide-based composites”. In: *Intermetallic Matrix Composites: Properties and Applications* (Jan. 2018), pp. 95–146. DOI: `10.1016/B978-0-85709-346-2.00005-4`.

[59] Yingjie Qiao, Hexin Zhang, Changqing Hong, and Xiaohong Zhang. “Phase stability, electronic structure and mechanical properties of molybdenum disilicide: a first-principles investigation”. In: *Journal of Physics D: Applied Physics* 42.10 (2009), p. 105413.

[60] H. Okamoto. “Mo-Si (Molybdenum-Silicon)”. In: *Journal of Phase Equilibria and Diffusion* 32 (2 Apr. 2011), p. 176. ISSN: 15477037. DOI: `10.1007/S11669-010-9843-0/TABLES/1`. URL: `https://link.springer.com/article/10.1007/s11669-010-9843-0`.

[61] M Samadzadeh, C Oprea, H Karimi Sharif, and T Troczynski. “Comparative studies of the oxidation of MoSi2 based materials: Low-temperature oxidation (300–900 C)”. In: *International Journal of Refractory Metals and Hard Materials* 66 (2017), pp. 11–20.

[62] S Zhang and ZA Munir. “Synthesis of molybdenum silicides by the self-propagating combustion method”. In: *Journal of materials science* 26.13 (1991), pp. 3685–3688.

[63] SC Deevi. “Self-propagating high-temperature synthesis of molybdenum disilicide”. In: *Journal of materials science* 26 (1991), pp. 3343–3353.

[64] Mohammad Shafiul Alam. *Combustion synthesis of molybdenum silicides and borosilicides for ultrahigh-temperature structural applications*. The University of Texas at El Paso, 2014.

[65] KS Vecchio, Li-Hsing Yu, and MA Meyers. “Shock synthesis of silicides—I. experimentation and microstructural evolution”. In: *Acta metallurgica et materialia* 42.3 (1994), pp. 701–714.

[66] LH Yu and MA Meyers. “Shock synthesis and synthesis-assisted shock consolidation of suicides”. In: *Journal of materials science* 26 (1991), pp. 601–611.

[67] BK Yen, T Aizawa, and J Kihara. “Synthesis and formation mechanisms of molybdenum silicides by mechanical alloying”. In: *Materials Science and Engineering: A* 220.1-2 (1996), pp. 8–14.

[68] RB Schwarz, SR Srinivasan, John J Petrovic, and CJ Maggiore. “Synthesis of molybdenum disilicide by mechanical alloying”. In: *Materials Science and Engineering: A* 155.1-2 (1992), pp. 75–83.

[69] Malek Ali and Marwa Liwa. “Modification of parameters in mechanochemical synthesis to obtain alpha-and beta-molybdenum disilicide”. In: *Advanced Powder Technology* 24.1 (2013), pp. 183–189.

[70] Timothy J Trentler, R Suryanarayanan, Shankar ML Sastry, and William E Buhro. “Sonochemical synthesis of nanocrystalline molybdenum disilicide (MoSi2)”. In: *Materials Science and Engineering: A* 204.1-2 (1995), pp. 193–196.

[71] S Govindarajan, B Mishra, DL Olson, JJ Moore, and J Disam. “Synthesis of molybdenum disilicide on molybdenum substrates”. In: *Surface and Coatings Technology* 76 (1995), pp. 7–13.

[72] Subhayu Choudhury. “A review of the sol-gel process and its application”. In: *International Education and Research Journal (IERJ)* 10.7 (July 2024). DOI: `10.21276/IERJ24449856325648`. URL: `https://ierj.in/journal/index.php/ierj/article/view/3547`.

[73] Linlin Guo, Xiaoxia Hu, Xin Tao, Haiyan Du, Anran Guo, and Jiachen Liu. “Low-temperature oxidation resistance of the silica-coated MoSi2 powders prepared by sol-gel preoxidation method”. In: *Ceramics International* 46 (15 Oct. 2020), pp. 23471–23478. ISSN: 0272-8842. DOI: `10.1016/J.CERAMINT.2020.06.117`.

[74] Lili Wu, Juan Yang, Xiangyang Zhou, Jingjing Tang, Yongpeng Ren, and Yang Nie. “Enhanced Electrochemical Performance of Heterogeneous Si/MoSi2 Anodes Prepared by a Magnesiothermic Reduction”. In: *ACS Applied Materials and Interfaces* 8 (26 July 2016), pp. 16862–16868. ISSN: 19448252. DOI: `10.1021/ACSAMI.6B04448/ASSET/IMAGES/LARGE/AM-2016-044485_0007.JPEG`. URL: `https://pubs.acs.org/doi/full/10.1021/acsami.6b04448`.

[75] Matt williams. *TG-DTA or TG-DSC Techniques for the Study of the Synthesis of Oxides by the Sol-Gel Method*. Accessed: 2024-12-04. URL: `https://www.spectraresearch.com/2015/03/21/tg-dta-or-tg-dsc-techniques-for-the-study-of-the-synthesis-of-oxides-by-the-sol-gel-method/`.

[76] Filip Ambroz, Thomas J Macdonald, Vladimir Martis, and Ivan P Parkin. “Evaluation of the BET Theory for the Characterization of Meso and Microporous MOFs”. In: *Small methods* 2.11 (2018), p. 1800173.

[77] Djalal Trache, M Hazwan Hussin, Caryn Tan Hui Chuin, Sumiyyah Sabar, MR Nurul Fazita, Owolabi FA Taiwo, TM Hassan, and MK Mohamad Haafiz. “Microcrystalline cellulose: Isolation, characterization and bio-composites application—A review”. In: *International Journal of Biological Macromolecules* 93 (2016), pp. 789–804.

[78] Alice Gualerzi, Silvia Picciolini, Cristiano Carlomagno, Francesca Roda, and Marzia Bedoni. “Biophotonics for diagnostic detection of extracellular vesicles”. In: *Advanced drug delivery reviews* 174 (2021), pp. 229–249.

[79] Guido Busca. “Infrared (IR) Spectroscopy”. In: *Springer Handbook of Advanced Catalyst Characterization*. Springer, 2023, pp. 3–32.

[80] L.M. Contreras, F.J.R. Jiménez, and M.A.R. Bribiesca. *IAEA Coordinated Research Project on Development of Harmonized QA/QC Procedures for Maintenance and Repair of Nuclear Instruments: Test Procedure for High Purity Germanium Radiation Detectors and Associated Electronics*. 2008.

[81] Scott C Wilschefski and Matthew R Baxter. “Inductively coupled plasma mass spectrometry: introduction to analytical aspects”. In: *The Clinical Biochemist Reviews* 40.3 (2019), p. 115.

[82] Geoff Tyler and J Yvon. “ICP-OES, ICP-MS and AAS Techniques Compared”. In: *ICP Optical Emission Spectroscopy Technical Note* 5 (1995).

[83] Deena Titus, E James Jebaseelan Samuel, and Selvaraj Mohana Roopan. “Nanoparticle characterization techniques”. In: *Green synthesis, characterization and applications of nanoparticles*. Elsevier, 2019, pp. 303–319.

[84] Raynald Gauvin. “Review of transmission electron microscopy for the characterization of materials”. In: *Materials Characterization and Optical Probe Techniques: A Critical Review* 10291 (1997), pp. 196–225.

[85] Brian Cantor. *The equations of materials*. Oxford University Press, 2020.

[86] Andrei A Bunaciu, Elena Gabriela UdriŞTioiu, and Hassan Y Aboul-Enein. “X-ray diffraction: instrumentation and applications”. In: *Critical reviews in analytical chemistry* 45.4 (2015), pp. 289–299.

[87] Jianguang Xu, Yu Zhang, Jinshun Qi, Yu Wang, Juhua Luo, and Wei Yao. “Preparation of nanocrystalline MoSi2 with enhanced lithium storage by sol–gel and carbonthermal reduction method”. In: *Ceramics International* 44.8 (2018), pp. 9494–9498.

[88] H. Putz and K. Brandenburg. *Match! - Phase Analysis using Powder Diffraction*. Kreuzherrenstr. 102, 53227 Bonn, Germany: Crystal Impact - Dr. H. Putz & Dr. K. Brandenburg GbR, 2025. URL: `https://www.crystalimpact.de/match`.

[89] TU Delft Reactor Institute. *Neutron Irradiation Facilities*. `https://www.tudelft.nl/tnw/zakelijk/faciliteiten/tu-delft-reactor-institute/diensten-consultancy/neutron-irradiation-facilities`. Accessed: 2024-10-17. n.d.

[90] Riya Gupta and Muhammad F Hashmi. “Mo99-Tc99m Generator”. In: *StatPearls* (2020).

[91] *Molybdenum dioxide*. ChemBK Website. Accessed: 2024-12-05. 2024. URL: `https://www.chembk.com/en/chem/Molybdenum%20dioxide`.

[92] Dale E Newbury and Nicholas WM Ritchie. “Performing elemental microanalysis with high accuracy and high precision by scanning electron microscopy/silicon drift detector energy-dispersive X-ray spectrometry (SEM/SDD-EDS)”. In: *Journal of materials science* 50 (2015), pp. 493–518.

[93] Alessandro Bertoluzza, Concezio Fagnano, Maria Antonietta Morelli, Vittorio Gottardi, and Massimo Guglielmi. “Raman and infrared spectra on silica gel evolving toward glass”. In: *Journal of Non-Crystalline Solids* 48.1 (1982), pp. 117–128.

[94] YQ Liu, G Shao, and P Tsakiropoulos. “On the oxidation behaviour of MoSi2”. In: *Intermetallics* 9.2 (2001), pp. 125–136.

[95] Jens Meyer, Sami Hamwi, Michael Kröger, Wolfgang Kowalsky, Thomas Riedl, and Antoine Kahn. “Transition metal oxides for organic electronics: energetics, device physics and applications”. In: *Advanced materials* 24.40 (2012), pp. 5408–5427.

[96] Liliia Molotovska, Dmytro Shakhnin, Natalia Uskova, Ganna Nikulina, Vladymyr Cherednik, Serge Stukota, and Viktor Malyshev. “Synthesis of VI group metals silicides dispersed powders by electrolysis of halide-oxide melts”. In: *J Chem Chem Eng* 1 (2016), pp. 7–12.

[97] Maximilian Yan, Sarah Martell, Siddharth V Patwardhan, and Mita Dasog. “Key developments in magnesiothermic reduction of silica: insights into reactivity and future prospects”. In: *Chemical Science* 15.39 (2024), pp. 15954–15967.

[98] Petra Martini, Licia Uccelli, Adriano Duatti, Lorenza Marvelli, Juan Esposito, and Alessandra Boschi. “Highly efficient micro-scale liquid-liquid in-flow extraction of 99mTc from molybdenum”. In: *Molecules* 26.18 (2021), p. 5699.

[99] JF Klopper, PDR Van Heerden, UD Muller, and WP Baard. “A simple automated system for the routine production of 99mTc by methyl-ethyl-ketone extraction”. In: *South African Medical Journal* 47.5 (1973).

[100] L Shaw and R Abbaschian. “Chemical states of the molybdenum disilicide (MoSi 2) surface”. In: *Journal of materials science* 30 (1995), pp. 5272–5280.

[101] G Daniel Todd, Sam Keith, Obaid Faroon, Melanie Buser, Lisa Ingerman, Courtney Hard, Mario J Citra, Amy Nguyen, Julie M Klotzbach, and Gary L Diamond. “Toxicological profile for molybdenum: draft for public comment”. In: *CDC Stacks* (2017).

[102] European Pharmacopoeia Commission. *Lutetium (177Lu) Solution for Radiolabelling*. 10.0. Chapter on Lutetium (177Lu) solutions, with details on radiolabelling applications, specifications, and quality standards. 2017.

[103] GP Haight and David R Boston. “Molybdenum species in aqueous solution—a brief summary”. In: *Journal of the Less Common Metals* 36.1-2 (1974), pp. 95–102.

[104] Sankha Chattopadhyay, Luna Barua, Sujata Saha Das, Anirban De, Umesh Kumar, Arpit Mitra, Tapas Mallick, Madhusmita, Md Alam Nayer, Samarendu Sinha, et al. “Pharmaceutical grade sodium [99m Tc] pertechnetate from low specific activity 99 Mo using an automated 99 Mo/99m Tc-TCM-autosolex generator”. In: *Journal of Radioanalytical and Nuclear Chemistry* 302 (2014), pp. 781–790.

[105] S Bulbulian. “Methyl ethyl ketone extraction of Tc species”. In: *Journal of radioanalytical and nuclear chemistry* 87 (1984), pp. 389–395.

[106] Daria Boglaienko, Odeta Qafoku, Ravi K Kukkadapu, Libor Kovarik, Yelena P Katsenovich, Denis E Cherkasov, Hilary P Emerson, and Tatiana G Levitskaia. “Elemental iron: reduction of pertechnetate in the presence of silica and periodicity of precipitated nano-structures”. In: *Environmental Science: Nano* 8.1 (2021), pp. 97–109.

[107] Joseph L Thompson and Warren W Miller. “Atomic and Ionic Recoil from the (n, γ) Reaction”. In: *The Journal of Chemical Physics* 38.10 (1963), pp. 2477–2479.

[108] Petra Martini, Alessandra Boschi, Licia Uccelli, Micol Pasquali, Adriano Duatti, A Salvini, L Strada, Giovanni Di Domenico, Gaia Pupillo, J Esposito, et al. “Extraction techniques of 99mTc from 100Mo metal target”. In: *Annual Report* (2013).

[109] William Reusch. *Virtual Textbook of Organic Chemistry - Solvents Used in Organic Chemistry*. `https://www2.chemistry.msu.edu/faculty/reusch/OrgPage/solvent.htm`. Accessed: 2024-12-16. 2024.

[110] Alan J Parker. “The effects of solvation on the properties of anions in dipolar aprotic solvents”. In: *Quarterly Reviews, Chemical Society* 16.2 (1962), pp. 163–187.

[111] Gauri. “Designing a Recyclable Low-Specific Activity 99Mo/99mTc Generator”. Unpublished work.

[112] Christopher D Williams, Karl P Travis, John H Harding, and Neil A Burton. “Selective Ordering of Pertechnetate at the Interface between Amorphous Silica and Water: a Poisson Boltzmann Treatment”. In: *MRS Online Proceedings Library (OPL)* 1744 (2015), pp. 53–58.

[113] Eshani Hettiarachchi and Vicki H Grassian. “Heterogeneous chemistry of methyl ethyl ketone on mineral oxide surfaces: impacts of relative humidity and nitrogen dioxide on product formation”. In: *Environmental Science: Atmospheres* 3.5 (2023), pp. 799–815.

[114] Fatma H El-Sweify, Alaa El-Din A Abdel Fattah, Ragaa El-Sheikh, Shorouk M Aly, and Mohamed A Ghamry. “Studies on 99Mo–99mTc adsorption and elution behaviors using the inorganic sorbent ceric tungstate and conventional organic resins”. In: *Radiochimica Acta* 105.7 (2017), pp. 561–568.

[115] Kovo G Akpomie, Jeanet Conradie, Kayode A Adegoke, Kabir O Oyedotun, Joshua O Ighalo, James F Amaku, Chijioke Olisah, Adedapo O Adeola, and Kingsley O Iwuozor. “Adsorption mechanism and modeling of radionuclides and heavy metals onto ZnO nanoparticles: a review”. In: *Applied Water Science* 13.1 (2023), p. 20.

[116] International Atomic Energy Agency (IAEA). *Product Issues with Eluted* ^{99m}*Tc*. `https://humanhealth.iaea.org/HHW/Radiopharmacy/VirRad/Eluting_the_Generator/Generator_Module/Elution_of_the_99Mo99mTc_generator/Product_issues_with_eluted_99mTc/index.html`. Accessed: 2024-11-27. n.d.

[117] TU Delft. `https://vips.tudelft.nl/rid/index.html`. Accessed: 2025-01-14.

[118] Geert-Jan de Haas. “The High Flux Reactor (HFR) - Nuclear Research at NRG”. In: *IAEA Consultancy Meeting on Catalogue of Research Reactors*. Vienna, Austria, June 2013. URL: `https://neutronsources.org/media/_a__haas_hfr_2013.pdf`.

Appendix A: Activity calculations

Figure A.1 and A.2 show screenshots from activity calculations performed using the VIPS software [117] at the Reactor Institute Delft. These calculations, based on neutron flux data from the High Flux Reactor at NRG Petten [118], were used to calculate the amount of $MoSi_2$ needed to produce approximately 1 Ci $^{99m}\mathrm{Tc}$.

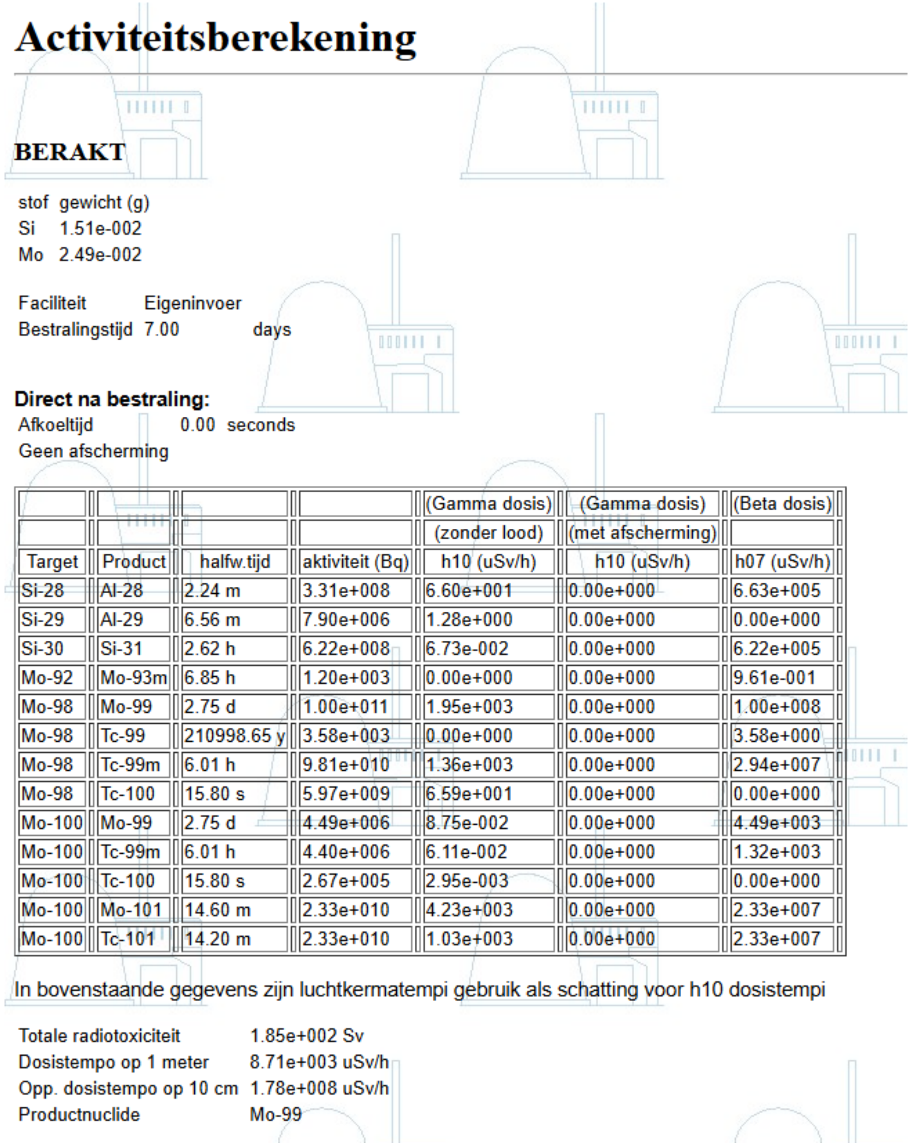

Activiteitsberekening

BERAKT

stof	gewicht (g)
Si	1.51e-002
Mo	2.49e-002

Faciliteit Eigeninvoer
Bestralingstijd 7.00 days

Direct na bestraling:
Afkoeltijd 0.00 seconds
Geen afscherming

				(Gamma dosis)	(Gamma dosis)	(Beta dosis)
				(zonder lood)	(met afscherming)	
Target	Product	halfw.tijd	aktiviteit (Bq)	h10 (uSv/h)	h10 (uSv/h)	h07 (uSv/h)
Si-28	Al-28	2.24 m	3.31e+008	6.60e+001	0.00e+000	6.63e+005
Si-29	Al-29	6.56 m	7.90e+006	1.28e+000	0.00e+000	0.00e+000
Si-30	Si-31	2.62 h	6.22e+008	6.73e-002	0.00e+000	6.22e+005
Mo-92	Mo-93m	6.85 h	1.20e+003	0.00e+000	0.00e+000	9.61e-001
Mo-98	Mo-99	2.75 d	1.00e+011	1.95e+003	0.00e+000	1.00e+008
Mo-98	Tc-99	210998.65 y	3.58e+003	0.00e+000	0.00e+000	3.58e+000
Mo-98	Tc-99m	6.01 h	9.81e+010	1.36e+003	0.00e+000	2.94e+007
Mo-98	Tc-100	15.80 s	5.97e+009	6.59e+001	0.00e+000	0.00e+000
Mo-100	Mo-99	2.75 d	4.49e+006	8.75e-002	0.00e+000	4.49e+003
Mo-100	Tc-99m	6.01 h	4.40e+006	6.11e-002	0.00e+000	1.32e+003
Mo-100	Tc-100	15.80 s	2.67e+005	2.95e-003	0.00e+000	0.00e+000
Mo-100	Mo-101	14.60 m	2.33e+010	4.23e+003	0.00e+000	2.33e+007
Mo-100	Tc-101	14.20 m	2.33e+010	1.03e+003	0.00e+000	2.33e+007

In bovenstaande gegevens zijn luchtkermatempi gebruik als schatting voor h10 dosistempi

Totale radiotoxiciteit	1.85e+002 Sv
Dosistempo op 1 meter	8.71e+003 uSv/h
Opp. dosistempo op 10 cm	1.78e+008 uSv/h
Productnuclide	Mo-99

Figure A.1: Activity calculations immediately after irradiation.

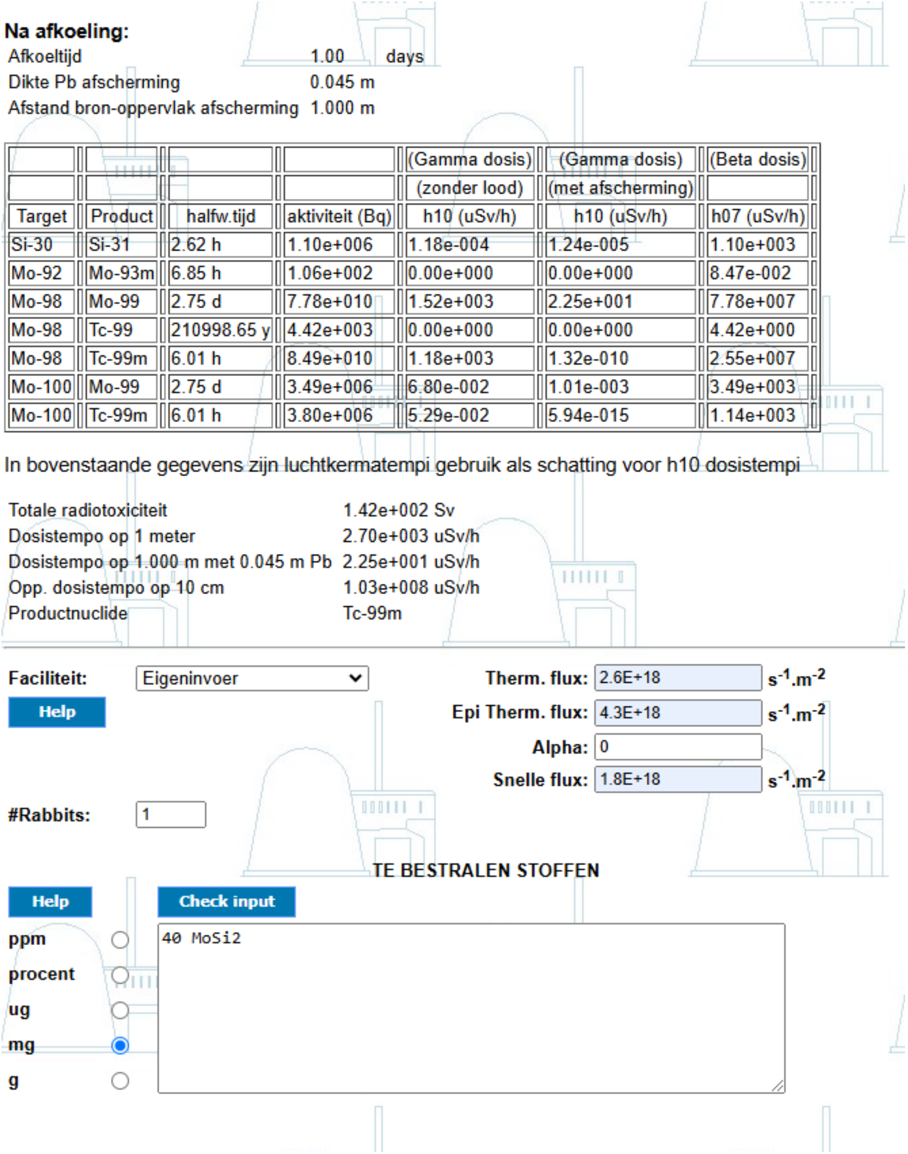

Na afkoeling:

Afkoeltijd	1.00	days
Dikte Pb afscherming	0.045 m	
Afstand bron-oppervlak afscherming	1.000 m	

				(Gamma dosis)	(Gamma dosis)	(Beta dosis)
				(zonder lood)	(met afscherming)	
Target	Product	halfw.tijd	aktiviteit (Bq)	h10 (uSv/h)	h10 (uSv/h)	h07 (uSv/h)
Si-30	Si-31	2.62 h	1.10e+006	1.18e-004	1.24e-005	1.10e+003
Mo-92	Mo-93m	6.85 h	1.06e+002	0.00e+000	0.00e+000	8.47e-002
Mo-98	Mo-99	2.75 d	7.78e+010	1.52e+003	2.25e+001	7.78e+007
Mo-98	Tc-99	210998.65 y	4.42e+003	0.00e+000	0.00e+000	4.42e+000
Mo-98	Tc-99m	6.01 h	8.49e+010	1.18e+003	1.32e-010	2.55e+007
Mo-100	Mo-99	2.75 d	3.49e+006	6.80e-002	1.01e-003	3.49e+003
Mo-100	Tc-99m	6.01 h	3.80e+006	5.29e-002	5.94e-015	1.14e+003

In bovenstaande gegevens zijn luchtkermatempi gebruik als schatting voor h10 dosistempi

Totale radiotoxiciteit	1.42e+002 Sv
Dosistempo op 1 meter	2.70e+003 uSv/h
Dosistempo op 1.000 m met 0.045 m Pb	2.25e+001 uSv/h
Opp. dosistempo op 10 cm	1.03e+008 uSv/h
Productnuclide	Tc-99m

Faciliteit: Eigeninvoer

Therm. flux: 2.6E+18 $s^{-1}.m^{-2}$

Epi Therm. flux: 4.3E+18 $s^{-1}.m^{-2}$

Alpha: 0

Snelle flux: 1.8E+18 $s^{-1}.m^{-2}$

#Rabbits: 1

TE BESTRALEN STOFFEN

ppm ○
procent ○
ug ○
mg ●
g ○

```
40 MoSi2
```

Figure A.2: Activity calculations after cooling.